UCRL-9288 Rev.

University of California

Ernest O. Lawrence Radiation Laboratory

Berkeley, California

DISCLAIMER

For Journal--Phys. Rev.

UCRL-9288 Rev.

UNIVERSITY OF CALIFORNIA

Lawrence Radiation Laboratory
Berkeley, California

Contract No. W-7405-eng-48

ANTIPROTON-NUCLEON CROSS SECTIONS FROM 0.5 to 1.0 Bev

Tommy Elioff, ~~Louis~~ Lewis Agnew, Owen Chamberlain, Herbert M. Steiner
Clyde Wiegand, and Tom Ypsilantis

December 12, 1961

UCRL-9288 Rev.

University of California

Ernest O. Lawrence Radiation Laboratory

Berkeley, California

Antiproton-Nucleon Cross Sections from 0.5 to 1.0 Bev

Contents

Antiproton-Nucleon Cross Sections from 0.5 to 1.0 Bev

Tommy Elioff, Louis Agnew,* Owen Chamberlain, Herbert M. Steiner
Clyde Wiegand, and Tom Ypsilantis

Lawrence Radiation Laboratory
University of California
Berkeley, California

December 12, 1961

ABSTRACT

Antiproton-production and nucleon-interaction cross sections were investigated for antiprotons in the energy range 0.5 to 1.0 Bev. The antiprotons were distinguished from other particles produced at the Bevatron by a system of scintillation- and velocity-selecting Cerenkov counters. The excitation function and momentum distribution were recorded for antiproton production in carbon and compared with statistical model expectations.

The antiprotons were directed by a system of bending and focusing magnets to a liquid hydrogen target. An array of plastic scintillation counters, which almost completely surrounded the hydrogen target, was used to determine the $\bar{p}$-p total, elastic, inelastic, and charge-exchange cross sections. Near 500 Mev the total $\bar{p}$-p cross section is about 120 mb, and it slowly decreases to 100 mb near 1 Bev. The inelastic cross section, which is principally due to the annihilation process, represents nearly 2/3 of the total cross section. The elastic scattering distribution is highly peaked in the forward direction and can be fitted by an optical model.

The total and partial cross sections were also determined for the collisions of antiprotons with deuterons. The $\bar{p}$-d total and inelastic cross sections were found to be approximately 1.8 times the $\bar{p}$-p cross sections. Corrections were

made for the shielding of nucleons within the deuteron in order to ascertain the $\bar{p}$-n interaction. The results indicate that the $\bar{p}$-p and $\bar{p}$-n cross sections are very nearly equal in this energy region, and that they satisfy the inequalities required by charge independence.

Antiproton-Nucleon Cross Sections from 0.5 to 1.0 Bev.

Tommy Elioff, ~~Louis~~ Lewis Agnew, Owen Chamberlain, Herbert M. Steiner
Clyde Wiegand, and Tom Ypsilantis

Lawrence Radiation Laboratory
University of California
Berkeley, California

December 12, 1961

I. INTRODUCTION

This report presents our final results in the investigation of antiproton-nucleon cross sections in the energy range 534 through 1068 Mev. By cross sections, we mean the total (σ_t), elastic (σ_e), inelastic (σ_i), and charge-exchange (σ_c) cross sections. Inelastic cross section here is synonymous with annihilation cross section for antiproton kinetic energies below the threshold (288 Mev) for pion production. Above 288 Mev, the inelastic cross section includes both annihilation and pion production (without annihilation). A preliminary report of the $\bar{p}$-p results has been given.[1] A portion of our results, together with a survey of other recent antinucleon experiments, is contained in reports by O. Chanberlain[2] and W. A. Wenzel.[3]

The particular energy range for antiprotons here was selected to extend the lower energy measurements of others[4,5,6,7] as well as to explain an apparent contradiction in previous results near 500 Mev. From the results of earlier experiments,[8,9] one would conclude that there was little diffraction scattering, whereas the inelastic cross section was very nearly the total cross section. In sharp contrast, the subsequently determined low-energy results (0 to 200 Mev) displayed a forward diffraction peak, and one found $\sigma_e \approx \sigma_i$. The low-energy results were in good agreement with calculations by Ball and Chew based on

conventional Yukawa pion-exchange mechanism.[10] While these calculations are not applicable above 250 Mev, a plausible model of the $\bar{p}$-p interaction advanced by Koba and Takeda[11] indicated a similar behavior at the energies under investigation here.

In addition to the basic cross-section measurements we have determined the angular distribution of $\bar{p}$-p elastic scattering at forward angles. These results are compared with an optical model. For the $\bar{p}$-p inelastic process the amount of pion production included with the annihilation in the total inelastic cross section has been estimated.

A further purpose of this experiment was to measure $\bar{p}$-d (antiproton-deuteron) cross sections and thus obtain the $\bar{p}$-n cross sections by a subtraction procedure between $\bar{p}$-d and $\bar{p}$-p data. Comparison of the $\bar{p}$-p and $\bar{p}$-n results reveals the amount of interaction in the two possible isotopic spin states of the nucleon-antinucleon system. These results are given in Sec. VI.

While it had been hoped that some information on antiproton production cross sections in hydrogen could be obtained, it was not possible to assure that the CH_2 target and the carbon target used within the Bevatron were irradiated identically by the Bevatron beam. Some comments are included in Sec. IV on the attempt to measure production in hydrogen. Results for production in carbon, such as the excitation function and momentum distribution of antiprotons, are presented.

II. APPARATUS

A. Antiproton Beams

The antiproton component of the beam was electronically selected from a momentum-analyzed beam of negatively charged particles—predominantly pions. The magnetic channel that formed the momentum-analyzed beam was similar to those of previous experiments.[12,13] Our system differed in that it was physically longer, and the momentum spread of particles traversing the channel was slightly larger. Specifically, the five energies utilized were 534, 700, 816, 948, and 1068 Mev.

A schematic diagram of the experimental area is shown in Fig. 1, and its principal components are identified in Table I. The Bevatron internal proton beam strikes either a carbon or polyethylene target T. The beam duration is approximately 100 msec. To obtain $\bar{p}$ beams of the five desired energies through our fixed system of magnets, we utilized several target positions (T) in the Bevatron magnetic field region. This allowed observation of antiprotons at small laboratory angles, which was desirable for obtaining maximum intensity. Three positions were found (at each position a carbon and a polyethylene target were used alternately) for which the magnetic channel would transmit antiprotons in the desired momentum range with laboratory angles of emission between 0 and 4 deg.

We will not elaborate on the magnetic channel, as details of our particular system here have been presented in reports by Chamberlain[14] and Ticho.[15] The general characteristics of the beam produced by this system may be described by momentum spread $\Delta p/p$ of $\pm$ 3%. For this interval, approximately 10^5 pions and 5 antiprotons were transmitted through the channel for each Bevatron pulse, during which nominally 7×10^{10} protons were incident on the Bevatron target T. More precise production rates are given in Sec. IV.

In order to view the beam size and position initially, and thereafter to be certain that all magnet currents were correctly set when alternating between various Bevatron targets and different antiproton momenta, we used a device called the Beam Profile Indicator to observe the beam-intensity distribution visually at any point in the magnetic channel. Basically, the Indicator is a row of 21 plastic scintillator elements. Each scintillator has a 1-cm^2 area perpendicular to the beam direction and is viewed by an RCA 1P21 photomultiplier tube. When particles traverse the scintillators, the proportionate accumulated charge from each photomultiplier current is sequentially displayed on an oscilloscope where the beam intensity pattern appears as a histogram (this device is described in detail elsewhere[16]). A typical beam pattern is shown in Fig. 2. The device could be inserted at desired positions along the beam and could also be rotated about the beam direction to obtain the profile in any plane through the beam direction.

B. Beam Counters

The counter system used to select antiprotons from the momentum-analyzed beam of negatively charged particles consisted of three scintillation counters, S_1, S_2, S_3 and two Cerenkov counters, VSC-II and $\bar{C}$. The positions of these counters along the beam are shown in Fig. 1, and their dimensions are given in Table I. The three scintillators were viewed by RCA 7264 photomultiplier tubes. Time-of-flight measurement between these counters rejected 99% of the pions. Effective discrimination against the remaining pions was obtained with the Cerenkov counters shown schematically in Fig. 3.

VSC-II was a narrow-band velocity selector tuned to antiproton velocity, and similar to the velocity-selecting Cerenkov counter described by Wiegand and Chamberlain.[17] The function of $\bar{C}$ was to detect particles having velocities greater than that of the antiproton (i.e., electrons, pions, muons). Thus $\bar{C}$ was used in anticoincidence. As described in the following paragraphs, it was possible to use the same Cerenkov radiator for both VSC-II and $\bar{C}$.

When a charged particle of velocity β traverses the radiator, which has an index of refraction n, Cerenkov light is emitted at an angle θ with respect to the particle direction, where θ is given by the expression

$$\cos \theta = \frac{1}{n\beta} . \qquad (1)$$

As seen in Fig. 3, the refracted light then leaves the radiator at angle θ', and is then guided by the cylindrical mirror and the three plane mirrors (arranged in a triangle) to the photomultiplier tubes. The plane mirrors merely serve to remove the tubes from the beam. Light emitted by a particle of given β reaches the photomultipliers only when the radiator, cylindrical mirror, and photomultipliers

have the proper separation governed by the angle θ'. These components slide on rails so that the counter can be easily adjusted for different velocities. The entire instrument is contained in a light-tight box. The light from particles slower or faster than the desired velocity misses the cylindrical mirror and is absorbed by the baffle or the outer black box. Accidental counts are minimized by the requirement that all three photomultipliers give an output in coincidence.

Figure 4 shows the efficiency for two particular velocity settings (indicated by arrows) of VSC-II, corresponding to antiprotons having momenta of 1200 Mev/c and 1640 Mev/c. The curves were obtained by sending protons of different velocities down the magnetic channel. The efficiency is defined as the ratio of the fourfold coincidence $S_1S_2S_3$ VSC-II to the threefold coincidence $S_1S_2S_3$.

The VSC-II radiator material was cyclohexene, contained in a thin-walled lucite cylinder 3.25 in. diam by 4.7 in. long. Cyclohexene ($CH{:}CH(CH_2)_3CH_2$) was chosen because of its low density (0.81 g/cc), its inability to scintillate, and chiefly because its refractive index was suitable for the combination of VSC-II and $\bar{C}$. The optical index of cyclohexene is 1.46 at wavelength 4250 Å. This is the average useful wavelength estimated from the response of the RCA 7046 photomultiplier to the portion of the Cerenkov radiation spectrum transmitted through the lucite container of the radiator and the lucite light pipe on the photomultiplier tube.

Although VSC-II and $\bar{C}$ are independent counters, they utilize the same Cerenkov radiator. This is possible for a radiator with index of refraction $(n) > \sqrt{2}$. For this case, total internal reflection occurs for the Cerenkov light from particles faster than a certain velocity β'. Specifically for $n = 1.46$, one finds $\beta' = 0.95$. The antiprotons detected by VSC-II were in the velocity range $0.7 \lesssim \beta \lesssim 0.9$, while pions of the same momenta have $\beta \gtrsim 0.99$. Thus total internal reflection occurs

for the Cerenkov radiation emitted by the pions, and this light is trapped within the radiator. In order to vent this pion light and at the same time accept negligible light from the antiprotons, a lucite light pipe was optically connected to the front end of the radiator and coupled to another photomultiplier tube. The setup is displayed in Fig. 3. Most of the light from the pions, perhaps after several reflections around the radiator, eventually reaches the 6810A photomultiplier tube. This is the $\bar{C}$ counter which, when used in anticoincidence with S_1, S_2, and S_3 (delayed for pions), rejected all but 0.015% of the pions.

C. Antiproton Interaction Detection System

Figure 5 shows a portion of the target assembly in relation to the counter system. The counter system consisted of 27 scintillation counters which almost completely surrounded the target flask. This flask could be filled with liquid hydrogen or deuterium.

The geometry of the counter system (Figs. 5 and 6) was designed to distinguish the various antiproton interaction processes. The basic idea is that the surrounding scintillators detect all out-going charged particles resulting from antiproton interactions within the target (similar to the method used by Coombes et al.[4]). Sixteen counters, designated S-1, S-2 ··· S-16, encircled the target like the staves of a barrel, while counters $\alpha, \beta, \gamma, \delta$, A, B, C, and D formed concentric rings in the forward direction when viewed from the target. S_4 and S_5 were good-geometry counters used for the total-cross-section measurements. These were constructed of 0.375-in.-thick plastic scintillators (97% polystyrene, 3% terphenyl, and 0.03% tetraphenyl butadiene), viewed by RCA 6810A photomultipliers.

Finally, the system was designed so that a layer of lead, approximately 0.375 in. thick (1.86 radiation lengths) in any radial direction from the target, could be inserted between the target and the scintillation counters in order to convert γ rays from the neutral pions resulting from antiproton annihilations.

A simplified block diagram of the basic electronics is shown in Fig. 7. The electronic identification of antiprotons was accomplished first by a fast coincidence of the scintillation counters S_1, S_2, and S_3 in anticoincidence with the meson counter $\bar{C}$. Another coincidence circuit received the signals from the three VSC-II photomultipliers to produce the final VSC-II signal. Finally a third coincidence circuit placed VSC-II in coincidence with $S_1S_2S_3\bar{C}$, and thus signaled the transmission of an antiproton through the magnetic channel and its incidence on the hydrogen target. The pion-rejection rate, i.e., the ratio of pions counted accidentally to the total number of pions that pass through the system, was 3×10^{-8}. Since the ratio of pions to antiprotons was $\sim5\times10^{4}$, there was only one accidental pion in every 10^{3} electronically identified antiprotons. However, even further discrimination was obtained by the photographic method described below.

As schematized in Fig. 7, the signal from an identified antiproton, i.e., the output of the 2×10^{-8} coincidence, was put in coincidence with each of the counters surrounding the hydrogen target by means of the 27 two-channel coincidence circuits. Each of the 27 possible outputs was delayed sequentially with alternate polarities for oscilloscope presentation, and each output was gated to eliminate mutual interference. The identified $\bar{p}$ signal was also used to trigger a four-beam oscilloscope, which displayed the 27 two-channel coincidence outputs along with the beam counters used to produce the trigger. The drawing in Fig. 8(a)

shows the positions of all possible pulses. Traces 1 and 2 display the beam counters with the exception of VSC-II. Here the final discrimination against the remaining pion contamination was made by rejection of any event that had a $\bar{C}$ pulse, approximately one event in a thousand. Since S_2 and $\bar{C}$ had the same polarity, they were electronically gated so that an accidental S_2 pulse could not simulate $\bar{C}$, and vice versa. In addition, the time-of-flight criterion was made more stringent by the measurement of the relative positions of S_1, S_2, and S_3 to within 2 nsec. The pulses labeled M in Fig. 8(a) are timing markers used to identify the positions of the other pulses; τ_1 τ_2, and τ_3 are beam-spill-time indicators used to identify the Bevatron energy at which the antiproton was formed.

The oscilloscope traces were photographed on 35-mm film. As many as six events could be recorded during a Bevatron pulse without interference between the various traces. Figure 9(b) is an actual photograph of the film in which five events are seen. The top trace of each of the four groupings is the first event.

III. PROCEDURE

When liquid hydrogen was used as the target material, it was surrounded by the lead converter (see Fig. 5) approximately half the time. The lead was important to insure accuracy in the inelastic cross section, as well as to indicate what fraction of the inelastic cross section was due to annihilation. In either case, i.e., with or without lead, runs were made in sequence for the five selected antiproton momenta and, for each momentum, runs were made with the hydrogen target alternately full and empty. This same procedure was repeated with deuterium as the target material.

To obtain the desired statistical accuracy, it was necessary to have ~ 20,000 antiprotons incident on the target for each cross-section measurement. Information on $\bar{p}$ production, and on the $\bar{p}$-p (or $\bar{p}$-d) total cross sections, was electronically monitored during the experiment. In order to obtain the $\bar{p}$ partial-interaction cross sections, the oscilloscope film had to be analyzed.

Analysis of the film data was guided by the fact that antiprotons entering the hydrogen target can interact in three ways; by elastic scattering, annihilation or inelastic scattering, and charge-exchange. From low-energy data[4,5,6] we know that elastic scattering is peaked in the forward direction and that, upon annihilation, 4.8 π mesons (about 2/3 of them charged) are produced on the average. Therefore, half the interaction detection counters (Figs. 5 and 6) surrounded the target in order to detect the major fraction of the annihilation pions. The remaining counters in the forward direction detected elastically scattered antiprotons as well as some of the annihilation pions. The central disc counters S_4 and S_5 monitored the noninteracting antiprotons. Information photographed on the oscilloscope (Fig. 8) was therefore classified as follows:

(a) Pass-throughs. If the good-geometry counters, S_4 and/or S_5 were the only counters that signaled, the antiproton passed through the hydrogen without interaction.

(b) Elastic scattering. If a single counter of the small-angle rings counted, it was considered an elastic scattering event, since the recoil proton did not have sufficient energy to leave the target. However, in the larger rings it was possible to have an additional counter signal due to the recoil proton. This event was accepted as an elastic scattering only if the event was coplanar within the resolution of the system.

(c) Inelastic scattering or annihilation. This classified events in which any three or more counters signaled. It also included those two-counter events whose geometry was inconsistent with elastic scattering.

(d) Charge exchange. This final classification was for the events in which none of the surrounding counters gave a signal, and therefore an event of the type $\bar{p} + p \rightarrow \bar{n} + n$ was assumed to have taken place.

A test was made to prove our system indeed capable of distinguishing between the classifications listed above. This test consisted of measuring known proton-proton cross sections. Positive proton beams were formed by scattering a 1.2-Bev internal Bevatron beam from an additional target located in the region T (see Fig. 1). With all magnet currents reversed, the p^+ traversed the magnetic channel and entered the hydrogen target in precisely the same manner as the $\bar{p}$. If the system could separate p-p elastic scattering from p-p inelastic events normally producing only one pion at these energies, it should easily distinguish $\bar{p}$-p elastic scattering from $\bar{p}$-p inelastic events in which up to 8 pions can be produced upon annihilation. The p-p total, elastic, and inelastic cross sections were measured at 528 and 940 Mev. The results, which have been presented in Table III of reference 1, were found to be in excellent agreement with previously measured p-p cross sections.

IV. ANTIPROTON PRODUCTION

A. Production in Hydrogen

It seemed possible that the cross section for antiproton production in p-p collisions might be measured (by a CH_2-C subtraction) at the same time the $\bar{p}$-interaction cross sections were being measured. The relatively high production rate in hydrogen indicated by a previous experiment[12] served as incentive to explore the production phenomenon more accurately here. Because an external proton beam at the Bevatron does not exist, we approached this phase of the experiment by utilizing the Bevatron internal beam. It was therefore necessary to use target materials such as C and CH_2 and resort to a subtraction process as before.

To ensure greater reliability in the subtraction process, target flipping mechanisms were developed to flip either the C or the CH_2 targets to identical positions within the Bevatron. The C and CH_2 targets themselves were designed to possess the same number of carbon atoms and at the same time have identical external physical dimensions. This was accomplished by cutting holes in the carbon target. A primary lip[18] was installed ahead of the desired target at a distance corresponding to the half-wave length of Bevatron radial oscillations. Heavy clipping devices were also stationed around the Bevatron tank to ensure negligible probability that the internal beam protons would hit the target holders, and that they would be stopped after one traversal of the target. To minimize unknown systematic effects of the Bevatron beam, the C and CH_2 were used alternately on each Bevatron pulse.

To determine the Bevatron radial position of the primary lip, observed production in the target was calculated approximately as a function of the lip radius. It had been expected that the characteristic shape of this curve would

indicate a lip position at which the protons would be focused onto the target T (Fig. 1). Unfortunately, there was no agreement between the calculated curve and the observed effect, so it was not possible to guarantee that both CH_2 and C targets were equally irradiated. If the targets themselves were acting to any appreciable extent as their own lips, then the effectiveness of the proton beam in penetrating the targets would have been subject to variations due to minute misalignments.

Our results showed that the CH_2 target was only 95% as effective as the carbon target (with the same number of carbon atoms) for producing 1684 Mev/c antiprotons at 0 deg. Owing to possible errors in this phase of the experiment, it is difficult to make a quantitative estimate of production in hydrogen. Even with a correction for absorption in targets, our results are consistent with no production of antiprotons from hydrogen. Thus, serious doubt is cast on the earlier results for 1190 Mev/c antiprotons, where production in hydrogen was found to be large with respect to production in carbon.[12] However, the present results are still indecisive due to uncertainties in Bevatron beam dynamics, and more accurate measurements must await external proton beams.

Apart from experimental difficulties, the above results might be explained by the particular $\bar{p}$ momentum chosen. Laboratory momentum 1684 Mev/c was used because antiprotons of this momentum have a velocity equal to the c.m. velocity resulting from 6-Bev nucleon-nucleon collisions. From a statistical calculation of the antiproton c.m. momentum distribution, similar to the method used by Amaldi et al.,[19] one would expect the laboratory $\bar{p}$ momentum distribution to peak at ~ 1684 Mev/c. Hagedorn has similarly calculated the antiproton c.m. momentum distribution;[20] however, he included the effect of final-state interactions

in which the $\bar{p}$ can annihilate with one of the three final-state nucleons. In the c.m. system, antiprotons having small relative momentum with one of the nucleons would be expected to be most susceptible to annihilation. This reduces the observed number of low-energy antiprotons in the c.m. system, and hence those in the laboratory system, at ~ 1684 Mev/c. Unfortunately, exploration of the CH_2 - C difference was not undertaken at momenta other than 1684 Mev/c.

B. Production in Carbon

The only previous information on the production of antiprotons as a function of Bevatron energy consisted of three experimental points for 1200-Mev/c antiprotons produced in a copper target.[21] This information was not sufficient to determine the shape of the excitation function. In Fig. 9 we present the results of this experiment for the production of 1684-Mev/c antiprotons. The experimental points were determined by counting the antiprotons traversing our magnetic channel and monitoring the Bevatron internal beam incident on our carbon target by means of the Bevatron induction electrodes. Corrections were made for detection efficiency, transmission through the magnet system, and absorption by material in the beam; therefore, the experimental points actually refer to production at the Bevatron target. These corrections introduce some uncertainty in the absolute cross section. Only the relative statistical errors are shown in Fig. 9.

Our data can be compared with the statistical calculations of Amaldi et al.,[19] who assumed that in a nucleus such as carbon, the principle antiproton production processes are:

$$p + n \rightarrow \bar{p} + p + p + n; \qquad (2)$$

and

$$p + p \rightarrow \bar{p} + p + p + p . \qquad (3)$$

For these reactions, the cross section was considered to be proportional only to the volume of phase space available. The kinetic energy available in the center-of-mass system is distributed among the four final-state particles according to statistical factors. The nucleons in the nucleus were considered to be a completely degenerate Fermi gas with maximum energy of 25 Mev. The following formula resulted for the laboratory distribution of antiprotons as a function of their momentum and angle, and also of incident proton energy:

$$S_n(p,\mu)dp\,d\mu = \frac{105}{16}\,\frac{p^2}{(p^2+1)^{1/2}}\,dp\,d\mu$$

$$\int_{4.0}^{W_{0\,max}} \frac{P(W_0)\,(W_0-4)^n\left[1-\left(\frac{p^*}{p^*_{max}}\right)^2\right]^2\left[(p^*)^2+1\right]^{1/2}\,dW_0}{(p^*_{max})^3}, \qquad (4)$$

where

W_0 = the total energy in the c.m. system (in proton mass units m_p),

$(W_0-4)^n$ = phase-space volume, where $n = 7/2$ for reaction (2), and $9/2$ for reaction (3),

p^* = antiproton c.m. momentum,

p = antiproton laboratory-system momentum,

μ = $\cos\theta$, where θ is the laboratory angle of emission of the $\bar{p}$ with respect to the forward direction,

and

$P(W_0)dW_0$ = the probability that W_0 (in the c.m. system) of the incident nucleon, and one nucleon in carbon, lies between W_0 and $W_0 + dW_0$.

We have evaluated $S_n(p = 1684 \text{ Mev/c}, \mu = 1)$ as a function of incident proton energy for the two cases $n = 5/2, 7/2$. The results are plotted in Fig. 9 along with the experimental data. A rather arbitrary normalization of the calculated results has been made with the experimental point at 5.1 Bev.

It is seen that the experimental values do not increase as rapidly as expected with increasing energy, since a value of n between 7/2 and 9/2 is predicted for Eqs. (2) and (3) in a purely statistical model. Thus the assumption of the statistical model may not be completely valid. Other types of nuclear models might be more appropriate for computing the function $P(W_0)$. It is also true that if other processes are important, aside from Eqs. (2) and (3) — such as the formation of a deuteron or helium nucleus in the final state — a smaller value for n in accordance with the experimental data would be predicted. Reports from CERN show that an appreciable number of deuterons, as well as some He^3, are produced in 24-Bev proton collisions.[22, 23]

In Fig. 9 one sees that the threshold for antiproton production in carbon is about 4.3 Bev. This would be expected from processes (2) and (3) when the target nucleons have a maximum Fermi energy of 25 Mev, the value assumed in the statistical calculations. This feature lends support to the initial assumption that proton-nucleon collisions are primarily responsible here, as much lower thresholds would be noticed for reactions such as (5) and (6):

$$\pi^- + p \rightarrow \bar{p} + p + n ; \qquad (5)$$

$$\pi^+ + n \rightarrow \bar{p} + p + p . \qquad (6)$$

Such processes can occur through a two-step process within the carbon target if a high-energy pion is first made by a proton-nucleon collision. This pion then proceeds to initiate reactions (5) and (6). The threshold at the Bevatron to produce a pion of sufficient energy in carbon (again assuming 25 Mev for the maximum Fermi

energy) is about 3.2 Bev. As no antiprotons were detected at our lowest energy of 4.25 Bev, our results show no evidence for reactions (5) and (6).

Data on the production of antiprotons as a function of their momenta are given in Table II, where information from other experiments is also presented for comparison.[9, 4, 24] Table II (fifth col.) gives the ratio of pions transmitted through the magnetic channel to incident protons on the target. This ratio is presented to show that the number of transmitted pions vs momentum is relatively constant in any given experimental arrangement, and that one is therefore able to use the pions to monitor the relative $\bar{p}$ rates. For col. 7 of Table II we have calculated the more desirable ratio of antiprotons to incident protons. These numbers have been corrected for counting efficiency and losses along the magnetic channel, so that they actually refer to antiprotons produced at the carbon target. Although the relative values of $\bar{p}/p^+$ are probably accurate, there is about a 20% uncertainty in the absolute p^+ monitor. Because of this factor, and differences in the targets as well as in the solid angles of acceptance and transmissions of the various spectrographs, this ratio is not tabulated for the other experiments listed in the table.

In Fig. 10, experimental data are again compared with statistical results.[19] The curve shown is obtained from Eq. (4) for $n = 7/2$, $T_{p^+} = 6.1$ Bev, and $\theta = 0$ deg, and it is normalized to the experimental point at 1684 Mev/c. It is seen that the calculations have indicated the shape of the momentum distribution reasonably.

No precise quantitative results were obtained for the angular distribution of antiprotons produced at a given momentum. Qualitatively, we found in our momentum range that the production cross section at ~ 10 deg in the laboratory system was about 12% smaller than the cross section at 0 deg.

V. ANTIPROTON-PROTON CROSS SECTIONS

A. Calculations and Results

The antiproton-proton interaction events, identified by the methods described earlier and classified according to the four categories enumerated in Sec. III, were used to calculate the fundamental $\bar{p}$-p cross sections by means of the following formulas:

$$\sigma_t = \frac{1}{N} \ln \left(\frac{I_0}{I} \times \frac{I'}{I_0'} \right), \tag{7}$$

$$\sigma_i = \frac{1}{N} \ln \left(\frac{I_0}{I_0 - I_i} \times \frac{I_0' - I_i'}{I_0'} \right), \tag{8}$$

$$\sigma_e = \frac{1}{N} \ln \left(\frac{I + I_e}{I} \times \frac{I'}{I' + I_e'} \right), \tag{9}$$

$$\sigma_c = \frac{1}{N} \ln \left(\frac{I + I_e + I_c}{I + I_e} \times \frac{I' + I_e'}{I' + I_e' + I_c} \right), \tag{10}$$

where

I_0 = the number of incident antiprotons,

I = the number of pass-throughs,

I_i = the number of inelastic events,

I_e = the number of elastic scatters,

I_c = the number of charge exchanges,

N = the number of protons/cm^2 in the target.

The unprimed quantities in the foregoing equations refer to measurements made with the hydrogen target full; the primed quantities refer to background measurements obtained with the target container empty.

The analysis of all the $\bar{p}$-p interaction events has yielded the results given in Table III for the five $\bar{p}$ energies investigated here. The results are practically the same as given in an earlier report in which ~ 60% of the data were analyzed.[1] Slight changes on the order of 1 to 2% seen in the table result from the inclusion of all the data; consequently, smaller errors are reported here.

The angular distribution of $\bar{p}$-p elastic scattering is shown in Figs. 11, 12, and 13. Most of the elastic scatters are contained within a cone of half-angle 40 deg (center-of-mass). Although our system could also detect the elastic scattering from 40 to 135 deg (center-of-mass), the angle θ could not be resolved in this case. The experimental points at 0 deg are lower limits determined by means of the optical theorem from the total-cross-section measurements. In Fig. 13 we have plotted the data of Armenteros et al. for comparison, who performed their experiment with techniques similar to this experiment,[24] but had better angular resolution, especially at large angles. The two sets of data are in very good agreement.

The curves shown in Figs. 11, 12, and 13 were calculated by means of the optical model of Fernbach, Serber, and Taylor,[25] in which the scattering amplitude, diffraction cross section, and absorption cross section are given respectively by

$$f(\theta) = \frac{1}{\lambda} \int_0^\infty (1-a)\, J_0\left(\frac{2\rho}{\lambda} \sin \frac{\theta}{2}\right) \rho \, d\rho , \qquad (11)$$

$$\sigma_e = 2\pi \int_0^\infty |\, 1-a \,|^2 \rho \, d\rho , \qquad (12)$$

and

$$\sigma_i = 2\pi \int_0^\infty (1 - a^2) \rho \, d\rho . \qquad (13)$$

For an incident wave of unit amplitude and zero phase, a is the amplitude and phase of the transmitted wave; ρ is of course the distance from the scattering center, measured in a plane orthogonal to the incident-wave direction. The particular ρ dependence of a used by Armenteros et al.[24] was

$$a = 0, \quad \text{for } 0 < \rho \leq R_0;$$
$$a = 1 - \exp\left[\frac{\rho^2 - R_0^2}{\rho_0^2}\right], \quad \text{for } \rho \geq R_0. \tag{14}$$

This corresponds to a black region of total absorption having radius R_0 surrounded by a region where the absorption decreases exponentially from R_0 with increasing ρ. The values of the parameters R_0 and ρ_0, determined from the experimental cross sections, appear in Table IV. The values from reference 24 are also shown. To obtain these parameters, our cross sections at 700 and 816 Mev were averaged for the calculation at 758 Mev, and those at 948 and 1068 Mev were combined to calculate the angular distribution at 1000 Mev. This was done because the angular distributions at these energies were nearly identical.

Owing to our lack of information at large angles, a comparison between various density distributions other than those in Eq. (14) is not feasible. It was shown, however, in reference 24, that the conditions of Eq. (14) give a better fit to the data at 980 Mev than a model of a completely grey region does.

It is of interest to consider the behavior of the inelastic cross section above the threshold for meson production. The inelastic cross section as defined earlier is due to the annihilation process below 288 Mev, while above this energy the following reactions may be included:

$$\bar{p} + p \rightarrow \bar{p} + p + \pi^0 , \quad (15)$$

$$\bar{p} + p \rightarrow n + \bar{p} + \pi^+ , \quad (16)$$

$$\bar{p} + p \rightarrow \bar{n} + p + \pi^- , \quad (17)$$

$$\bar{p} + p \rightarrow \bar{n} + n + \pi^0 . \quad (18)$$

(Double-pion production is negligible below 1 Bev, as is the case in the p-p and n-p interactions.[26]) These processes have the distinctive feature that only two charged particles are produced in the final state, except for process (18) in which the gammas from the π^0 decay might appear upon conversion as one or two charged particles; thus the analysis of our one- and two-particle inelastic events obtained with the lead converter allows us to estimate the cross section for (16), (17), and (18). The same procedure cannot be used for (15) without the lead converter, because this process is not distinguished by our counters from the more abundant annihilation mode

$$\bar{p} + p \rightarrow \pi^+ + \pi^- + n\,\pi^0 . \quad (19)$$

We find that inelastic processes (16), (17), and (18) taken together compose 5±3 mb of the inelastic cross section at each of the $\bar{p}$ energies of this experiment. This result is in agreement with the more accurate data of Xuong et al. for 930-Mev antiprotons in the Berkeley 72-inch hydrogen bubble chamber.[27] They obtain 1.6, 1.1, and 0.96 mb respectively for processes (15), (16), and (17).

B. Corrections and Uncertainties

The errors quoted in Table III are the standard deviations due to counting statistics together with the estimated uncertainty in the following corrections.

1. The Total Cross Section

The total cross sections were corrected for forward scattering. This was done by measuring the cross sections at three different cutoff angles (3, 4.2, and 5.3 deg) determined by counters S_4 and S_5. These results were plotted vs solid angle (determined by the cutoff angle) and extrapolated to zero solid angle by a straight-line least-squares fit. The result gave the same correction factor as one would obtain by using the optical theorem[28] and the assumption $d\sigma/d\Omega(0^\circ) \approx I_0^2$, where I_0 is the imaginary part of the forward-scattering amplitude. This correction factor (3 deg to 0 deg) amounted to approximately 2 mb.

Small corrections of the order of 1% to 2% have been made for accidentals and for annihilations in counters S_4 and S_5. The accidentals are due to the high flux of neutrons in the Bevatron experimental area. The concrete shielding around area A (Fig. 1) was not sufficient to eliminate this background entirely. To determine the accidental rate, a number of runs were made during which the $\bar{p}$ trigger from the 2×10^{-8} sec coincidence (Fig. 7) was put out of delay with respect to each of the 27 signals from the counters encircling the hydrogen target. The oscilloscope traces were photographed as in a normal run. Any pulses that occurred during this time were due to the accidental counts. The results showed that an average counter had a probability of $\sim1.5\times10^{-3}$ for counting accidentally during a real event. Corrections were made for this effect in the analysis of the various events.

2. Elastic-Scattering Cross Section

The same correction for forward scattering has been made as in the total cross section, as well as similar corrections for accidentals and annihilations in counters. An additional correction (~ 1%) has been made for scatterings that find their way through small cracks between counters and so simulate charge exchange.

No correction has been made for backward-scattered antiprotons that may not have sufficient energy to leave the target and hence annihilate in the hydrogen, because of the uncertainty in the angular distribution at large angles. However, other experiments, in which the angular distributions are known to large angles,[5,7,29] indicate that this correction is small ($\lesssim 1.0\%$).

3. Inelastic Cross Section

Here, corrections for annihilations in counters and for accidentals have also been made. We note that annihilation events of the type $\bar{p} + p \rightarrow \pi^+ + \pi^- + n\pi^0$ (where n is an integer of average value ~ 3) can be distinguished from elastic scattering chiefly because of the coplanarity condition. This was verified when the lead converter was used and the number of elastic scattering events remained unchanged. The particular annihilation mode, $\bar{p} + p \rightarrow \pi^+ + \pi^-$, cannot of course be distinguished from elastic scattering by our system. However, this mode has been estimated from bubble chamber experiments to constitute less than 0.3% of all annihilations.[5,26] The other possible annihilation modes are unambiguous.

4. Charge-Exchange Cross Section

For the charge-exchange cross sections, corrections have likewise been made for antineutron annihilations in the surrounding counters, for accidental events that would make a charge exchange appear as a pass-through or elastic scattering, and for the small fraction of small-angle elastic scatterings that would normally

be counted in only one counter, but can occasionally travel through a crack between counters and be recorded as a charge-exchange event. A correction has also been made for annihilations that produce π^0 mesons only. Previous experiments indicate that possibly 20% of the charge-exchange cross section (as determined here when the lead converter was not used) could be due to "zero-prong annihilations".[5,6] This amounts to about 1.5 mb. Low-energy theoretical calculations agree with this estimate,[30] and our results determined with lead converter corroborated an effect of about this size.

The data taken without lead converter included the process $\bar{p} + p \rightarrow \bar{n} + n + \pi^0$ as part of σ_c, while for the data with lead converter this process is recorded as part of σ_i. Since the cross section for this process is yet unknown, we have made no correction, however it is believed to be ~ 1 mb.[26,31]

C. Discussion

The results for the $\bar{p}$-p cross sections given in Table III are plotted in Fig. 14, to compare them with the cross sections obtained by others at nearby $\bar{p}$ energies.[4,5,8,9,6,24,32] One sees a reasonable transition between the low-energy cross sections and those determined by this experiment. There is excellent agreement between our highest-energy points and the data of reference 24. In the energy interval of this experiment the general trend of the $\bar{p}$-p cross sections is a slow decrease with increasing energy; the cross sections vary approximately as $T_{\bar{p}}^{-1/2}$, where $T_{\bar{p}}$ is the $\bar{p}$ laboratory-system kinetic energy. Although the charge-exchange cross section appears nearly constant, it is not inconsistent with the energy dependence of the other cross sections. Our values for the charge-exchange cross section are in agreement with other data (obtained by different methods) not presented in Fig. 14. For example, Weingart et al. obtained the value 10.9±5.8 mb

at 455 Mev.[33] They used a C and a CH_2 target to initiate the charge exchange and a large block of plastic scintillator to detect the antineutron annihilation. The experiment of Hinrichs et al. utilizing 930-Mev antiprotons in the 72-inch hydrogen bubble chamber has yielded a value of 7.8±0.6 mb for the charge-exchange cross section.[31]

We have discussed in a previous report the puzzling situation created by earlier experimental results near 500 Mev.[1] As seen in Fig. 14, these data indicated a large absorption cross section with little diffraction scattering.[8, 9] The situation seems largely resolved, as our present data show the diffraction scattering near 500 Mev to be ~ 1/3 of the total cross section.

In the antiproton energy range 50 to 250 Mev, the $\bar{p}$-p cross sections are understood in terms of the theory of Ball and Chew.[10] Their model stresses the analogy between the $\bar{p}$-p and the nucleon-nucleon systems. They use the Gartenhaus-Signell-Marshak potential,[34, 35] which seems to represent the nucleon-nucleon interaction up to about 200 Mev, and modify it suitably for the antinucleon case. The result is that a nucleon appears to an antiproton as black hole or core region, surrounded by a potential due to the pion cloud. The earlier experimental data (also shown in Fig. 14) lend support to this model. In the energy range of applicability, i.e., 50 to 250 Mev one finds $\sigma_e \approx \sigma_i \approx \sigma_t/2$. Thus the Ball-Chew model in its predictions is very nearly like a classical black-sphere region of size $\lambda\!\!\!^{-}_{\pi}$ (pion Compton wave length). This is explained by the effectiveness of the outer potential due to the pion cloud which draws the $\bar{p}$ into the core region where it annihilates.

The methods used in the Ball-Chew calculations render them inapplicable in our energy range. However, a model along the same trend of ideas has been proposed by Koba and Takeda.[11] Their predictions are applicable at our energies

and accord with our measured cross sections. Their model consists of a completely phenomenological core region surrounded by a pion cloud. The core region is likened to a black sphere whose radius a_0 is left as an adjustable parameter. Outside the core region is the potential owing to the pion could, which they surmise can be calculated in principle by meson theory at high energies in a manner perhaps similar to that of Ball and Chew for low energies. It is expected that the pion potential will become less effective as one approaches high energies, and the annihilation cross section should become πa_0^2. This feature has also been pointed out by Chew.[36] Koba and Takeda considered the effect of the core region alone. As the classical approach is not valid in the energy region 300 to 800 Mev, they solve the Schrödinger equation and obtain

$$\sigma_a = \pi (a_0 + \lambda)^2 \qquad (20)$$

for the annihilation cross section, instead of the classical result $\sigma_a = \pi a_0^2$. It is found that higher-order partial waves that classically would never reach the core can be partially absorbed; thus the absorption cross section is increased relative to the scattering cross section. Koba and Takeda find for $a_0 = 2/3\ \lambda_\pi = 0.94 \times 10^{-13}$ cm that the ratio of the elastic scattering cross section to the annihilation cross section is 1/2. From our experimental data in Fig. 14 one sees that σ_e/σ_i is 1/2 near 1 Bev, and only slightly larger at 534 Mev. The data for σ_i can very nearly be fitted by Eq. (20) for $a_0 = 0.95 \times 10^{-13}$ cm. For this value the high-energy points lie slightly above the curve, but this might be accounted for by a difference between σ_i and σ_a, because of pion production.

The optical-model analysis of the angular distributions of the $\bar{p}$-p elastic scattering indicates a rather large opaque nucleon structure. In the region near 300 Mev, the differential scattering can be fitted by a completely black region

of radius $\sim\lambda\!\!\!^{-}_{\pi}$. In the preceding section, it is seen that our data from 534 to 816 Mev can be fitted by a black region of radius $2/3\ \lambda\!\!\!^{-}_{\pi}$, surrounded by a region of decreasing grayness. Similar conditions exist up to 2 Bev, as shown in Table IV.

In view of the above observations it is not unreasonable to think of the $\bar{p}$-p interaction region as having a structure whose total size is $\sim\lambda\!\!\!^{-}_{\pi}$, within which the core region where annihilation taken place may be as large as $2/3\ \lambda\!\!\!^{-}_{\pi}$. While arguments from meson theory favor a smaller annihilation region of the order of $\lambda\!\!\!^{-}_{p} = (0.21\times10^{-13}$ cm),[37,38] Tamm has pointed out that a larger core region is within the realm of theoretical expectations.[39] Perhaps the determination of the $\bar{p}$-p partial cross sections in the multi-Bev region will yield further information on this point.

VI. DETERMINATION OF ANTIPROTON-NEUTRON CROSS SECTIONS

In order to understand the antinucleon-nucleon system completely, information must be acquired not only for the $\bar{p}$-p interaction, but also for the $\bar{p}$-n (or $\bar{n}$-p). As in the nucleon-nucleon case, one can then determine the amount of interaction in each of the two possible isotopic spin (I) states of the antinucleon-nucleon system. The $\bar{p}$-n system is purely I = 1 state, while the $\bar{p}$-p system exists with equal probability in both I = 1 and I = 0 states. Tests for the validity of charge independence can thus be made from a knowledge of the $\bar{p}$-p and $\bar{p}$-n cross sections.

The experimental factors involved in the determination of the $\bar{p}$-p cross sections are considerably more attractive than those for the $\bar{p}$-n or $\bar{n}$-p cross sections. For the former, $\bar{p}$ beams exist, hydrogen targets are at hand, and both particles involved are charged. In the latter, one is faced with the necessity of providing a neutron target or an antineutron beam, in addition to the difficult feature of detecting a neutral particle. The feasibility of obtaining antineutron beams utilizing the reaction $p + p \rightarrow \bar{n} + He^3$ was investigated by Moyer et al.,[40] the procedure was found very difficult. However, the use of antineutrons from the $\bar{p}$-p charge-exchange process seem to offer promise.[31]

The other alternative, chosen here, is to make indirect use of a neutron target via the deuteron. The hydrogen target used to obtain the $\bar{p}$-p cross sections in Sec. V was equally capable of containing deuterium, and a supply of antiprotons was at hand. Thus in principle, the subtraction of the $\bar{p}$-p cross sections from the $\bar{p}$-d cross sections could be made, and values for the $\bar{p}$-n cross section assessed. To this end we have determined the $\bar{p}$-d cross sections at the same five energies as the preceding p-p data. The $\bar{p}$-d data are presented first, as their validity seems secure because they are ascertained in the same manner as the $\bar{p}$-p results.

The subtraction procedure used for the $\bar{p}$-n values, subject to some uncertainty, is discussed in the subsequent section.

A. Antiproton-Deuteron Cross-Section

The various types of $\bar{p}$-d interactions i.e., scattering, annihilation, etc., were identified in the manner outlined in Sec. III. Calculation of the cross sections and correction factors was performed by the methods already mentioned for the $\bar{p}$-p cross sections. The results are listed in Table V and plotted in Fig. 15.

No distinction can be made by our detection system between elastic $\bar{p}$-d scattering and quasi-elastic $\bar{p}$-p or $\bar{p}$-n scattering. Observations of the corresponding p^+d reaction at 660 Mev[41] indicate, however, that the probability that the deuteron remains intact is quite small. Because of the predominant forward scattering, only about 20% of the scatterings are accompanied by a recoil proton with sufficient energy to escape the target. For the data taken without the lead converter some $\bar{p}$-p_d elastic scatters may not be distinguished from the $\bar{p}$-p_d two-charged-pion annihilation mode (see Eq. 19) because of the deuteron internal momentum (p_d refers to the bound proton within the deuteron). Comparison of runs with and without converter has shown, however, that the effect is within the limits of our statistical errors. The difference between lead in and lead out also revealed no ambiguity between the majority of the elastic scatterings, in which no recoil nucleon was detected, and the p-n_d one-charged-pion annihilation mode.

An additional small correction to the elastic scattering may result from the meson-production process (or inelastic charge exchange), $\bar{p} + n_d \rightarrow \bar{n} + n + \pi^-$. Judging from the magnitude of the cross section for similar processes in the $\bar{p}$-p case, one would not expect this reaction to be more than ~ 1.0 mb.[31]

From Fig. 15, it is seen that the energy dependence of the $\bar{p}$-d cross sections is very similar to the $\bar{p}$-p results. The total and inelastic cross sections are 1.8 times the corresponding $\bar{p}$-p cross sections, while the factor for elastic scattering is approx. 2.0. The charge-exchange cross sections are slightly smaller in deuterium. We recall that the charge-exchange process can occur only for the proton; consequently one might expect the same value for σ_c ($\bar{p}$-p) and σ_c($\bar{p}$-d). However, the shadow correction discussed in the next section would reduce σ_c($\bar{p}$-d) relative to σ_c ($\bar{p}$-p), as is observed. The only other existing datum for the $\bar{p}$-d reaction (obtained by Chamberlain et al.[8]) has also been plotted in Fig. 15. It is in agreement with our results.

B. Antiproton-Neutron Cross Sections

Experimental information on nucleon-deuteron and nucleon-nucleon cross sections at high energies (~ 1 Bev) indicates that the sum of free-nucleon cross sections is approximately 10% greater than the deuteron cross section. Thus a quantitative expression for the deuteron cross section, where x is the incident particle, must be written as

$$\sigma(x, d) = \sigma(x, p) + \sigma(x, n) - C, \qquad (21)$$

where C is a correction factor sometimes called the "eclipse" or "shadow" factor. This correction is due to the partial shielding of one nucleon by the other within the deuteron.

The shadow factor was studied in detail by Glauber.[42] By means of diffraction theory Glauber has calculated a general expression for C in terms of the outgoing-wave amplitudes and phases. In view of the lack of knowledge of these factors, he develops an approximate formula for the correction factor of the total cross sections,

$$C_t = \frac{4\pi}{k^2} \mathrm{Re} \left\{ f_p(0)\, f_n(0) \right\} \left\langle r^{-2} \right\rangle_d , \qquad (22)$$

where $f(0)$ refers to the forward scattering amplitude, r is the neutron-proton separation, and the angular parentheses refer to an average value in the deuteron ground state. The result of Eq. (22) is very similar to what one would obtain by a simple classical computation of the decrease of incident flux when one nucleon is in front of the other; however, the work of Glauber differs in that the coherent diffraction scattering of the two nucleons is taken into account. One of the major approximations made for the particular expression (22) is that r is larger than the nucleon-interaction range. Under the additional assumption of a purely absorptive interaction, Glauber obtains, for the total deuteron cross sections,

$$\sigma_t(x, d) = \sigma_t(x, p) + \sigma_t(x, n) - \frac{1}{4\pi} \sigma_t(x, p)\, \sigma_t(x, n) \left\langle r^{-2} \right\rangle_d . \tag{23}$$

For the absorption cross section the relation

$$\sigma_i(x, d) = \sigma_i(x, p) + \sigma_i(x, n) - \frac{1}{2\pi} \sigma_i(x, p)\, \sigma_i(x, n) \left\langle r^{-2} \right\rangle_d \tag{24}$$

is found. A similar expression for the scattering cross section can also be determined.[42]

To calculate the last term in the last two equations, the deuteron wave function must be known. Three different wave functions corresponding to a square-well potential, a Hulthen potential, and an attractive potential with a hard core were used previously to estimate $\sigma_t(\pi^- \text{-} d)$. The respective results for the last term in Eq. (23) were 4.2, 5.3, and 3.3 mb.[43] The experimental result in the pion energy range 0.79 to 1.5 Bev was found to be 6 ± 2 mb. For the nucleon-deuteron interaction near 1 Bev, the three wave functions above yielded correction factors of 5.7, 7.2, and 4.5 mb respectively.[44] Experimentally, the correction was found to be 7.4 mb. Thus for the particular cases mentioned the Glauber correction seems adequate.

Considerations of the same corrections in the circumstance where the incident particle is an antiproton result in extremely large shadow factors. This is because of the large size of the $\bar{p}$-p (and presumably the $\bar{p}$-n) cross sections in relation to the nucleon-nucleon cross section. The validity of the approximate Glauber formulas (Eqs. 23, 24) is in serious doubt, especially in view of the assumption that the radius of interaction is much smaller than the size of the deuteron.

J. S. Blair has calculated the shadow effect by means of a semiclassical model which does not require this last assumption.[45] It is therefore certainly more appropriate in the antinucleon case. For small values of the free-nucleon cross sections, the Blair calculations yield the same results as the approximate Glauber factors, and hence the same agreement for the π-d and p^+-d cross sections mentioned in the previous paragraphs. The disagreement with the approximate Glauber formulas becomes strongly apparent when the free-nucleon cross sections are 60 mb or greater, as in the case of antinucleons. The Blair calculations rest principally on the assumptions that the impulse approximation is valid, and that the interaction can be represented by a black disc. These calculations were made in anticipation of $\bar{p}$-d cross sections such as ours.

In Table VI, the Blair correction factors, C_i, for the inelastic or absorption cross sections are shown. The model for the deuteron used was the Hulthen wave function

$$\psi_d = \left[\frac{a}{2\pi}\,\frac{\beta(a+\beta)}{(a-\beta)^2}\right]^{1/2}\frac{\exp[-ar]-\exp[-\beta r]}{r}\,, \qquad (25)$$

with $\beta = 6a$, where $\beta = 3/\rho\,(1+\frac{4}{9}\,a\rho)^{-1}$, corresponding to a triplet effective range $\rho = 1.75\times10^{-13}$ cm. In the second column of the table we have the apparent neutron cross section "σ(p-n)" defined by the direct subtraction $\sigma(\bar{p}\text{-d})-\sigma(\bar{p}\text{-p})$, from the data of Tables III and V. The true or corrected neutron cross sections are shown in the final column.

The correction factors for the total or elastic cross sections merit additional consideration. Shielding of the absorption cross section is more easily understood because absorptive processes by the two nucleons are mutually exclusive events. In the total cross section other factors are involved, such as interference effects, double scattering, and scattering by one nucleon followed by absorption by the other. It is shown by Glauber[42, 46] that all these effects are taken into account by his general correction formula for σ_t, of which Eq. (23) is an approximation. The difference between the formula for the total cross section Eq. (23) and the one for the absorption cross section (Eq. 24) is simply a factor of 2. This difference is valid only for a purely absorptive interaction; however, it is independent of the opacity of the interaction region. In view of the use of the optical theorem in conjunction with the last assumption to obtain Eq. (23), the resulting correction to the total cross section should be a minimum correction. We therefore employ this factor of 2 together with the more explicit Blair results to obtain the total-cross-section corrections shown in Table VI. The elastic $\bar{p}$-n cross section was obtained by subtracting σ_i from σ_t. The results are plotted in Fig. 16 for a comparison with the $\bar{p}$-p values.

C. Conclusions

From the presentation in Fig. 16 it is seen that the $\bar{p}$-n and the $\bar{p}$-p cross sections are statistically the same within the energy interval of this experiment. It should be emphasized that this conclusion rests on the validity of the Blair correction factors employed to obtain the $\bar{p}$-n cross sections. These correction factors have not been experimentally proven for antinucleon cross sections as they have been for nucleon and pion cross sections. In view of the assumptions made in the derivations of the shielding factors,[42, 45] they are not expected to be entirely

accurate, but to provide a reasonable estimate. The shadow correction to the annihilation cross sections seems the most reliable, because fewer assumptions are involved. The other shadow corrections would seem to be more uncertain because of the assumption of a purely absorptive interaction with zero phase shift.

The equality of $\bar{p}$-p and $\bar{p}$-n cross sections may not be totally unexpected. The near equality is noted in the calculations by Ball and Fulco for antinucleons in the energy range 50 to 250 Mev.[47] Their theoretical results are based on the theory of Ball and Chew.[10] As the low-energy experimental results for the $\bar{p}$-p cross sections support the theoretical expectations, it would not be surprising for the $\bar{p}$-n cross sections to do likewise, although no experimental $\bar{p}$-n information exists at low energies.

The $\bar{p}$-p system may interact through the isotopic spin states I = 0 and I = 1 with equal probability. The $\bar{p}$-n, however, exists only in the I = 1 state. Thus within the limits of our errors, the equality of the $\bar{p}$-n and $\bar{p}$-p cross sections reveals that the antinucleon-nucleon interaction occurs in the I = 0 and I = 1 states with the same probability. There exist inequality relations between $\bar{p}$-p and $\bar{p}$-n cross sections which are independent of detailed nuclear models and require only the charge independence of nuclear forces. These inequalities follow from the fundamental relations of the scattering amplitudes between initial and final states of T = 0 and T = 1. The resulting expressions, which have been summarized in Reference 48, are as follows:

$$\frac{d\sigma_c(\bar{p}\text{-}p)}{d\Omega}(0^\circ) \geq (k/4\pi)^2 [\sigma_t(\bar{p}\text{-}n) - \sigma_t(\bar{p}\text{-}p)]^2 , \tag{26}$$

$$\sigma_e(\bar{p}\text{-}p) + \sigma_c(\bar{p}\text{-}p) \geq 1/2\, \sigma_e(\bar{p}\text{-}n) , \tag{27}$$

$$|\{\sigma_c(\bar{p}\text{-}p)\}^{1/2} - \{\sigma_e(\bar{p}\text{-}n)\}^{1/2}| \leq \{\sigma_e(\bar{p}\text{-}p)\}^{1/2} \leq \{\sigma_c(\bar{p}\text{-}p)\}^{1/2} + \{\sigma_e(\bar{p}\text{-}n)\}^{1/2} , \tag{28}$$

$$|\{\sigma_c(\bar{p}\text{-}p)\}^{1/2} - \{\sigma_e(\bar{p}\text{-}p)\}^{1/2}| \leq \{\sigma_e(\bar{p}\text{-}n)\}^{1/2} \leq \{\sigma_c(\bar{p}\text{-}p)\}^{1/2} + \{\sigma_e(\bar{p}\text{-}p)\}^{1/2} , \tag{29}$$

$$|\{\sigma_e(\bar{p}\text{-}n)\}^{1/2} - \{\sigma_e(\bar{p}\text{-}p)\}^{1/2}| \leq \{\sigma_c(\bar{p}\text{-}p)\}^{1/2} \leq \{\sigma_e(\bar{p}\text{-}n)\}^{1/2} + \{\sigma_e(\bar{p}\text{-}p)\}^{1/2} . \tag{30}$$

Relations (27) through (30) are satisfied by our data of Fig. 16. The first relation (Eq. 26) is satisfied by our value for σ_t (at 948 Mev) and a value 4.6 mb/sr for the differential charge-exchange cross section obtained by Hinrichs.[31] The antinucleon-nucleon data are therefore consistent with the relations required by charge independence in the energy range 500 to 110 Mev. For this relatively low energy range the data is also in accordance with the theorem of Pomeranchuk which states that the $\bar{p}$-p and the $\bar{p}$-n cross sections should become equal at high energies ' as a consequence of conservation of isotopic spin.[49] An additional theorem due to Pomeranchuk, based on the dispersion relations for elastic scattering of nucleons in the forward direction, states that the $\bar{p}$-p and the p-p cross sections should also be the same at 'high energies.'[50] At the energies under investigation here and in those of reference 24, the $\bar{p}$-p cross sections remain much larger than the p-p cross sections. Recent cross-section measurements up to 20 Bev/c show larger $\bar{p}$-p cross sections;[51, 52] however, the $\bar{p}$-p and p-p total cross sections seem to be approaching each other at higher energies.

ACKNOWLEDGMENTS

We wish to thank Professor Emilio Segrè for his support and advice, and Dr. Norman Booth for his aid in the successful operation of the experiment. The assistance of Mr. Bill Johnson and Mr. Olav Vik was appreciated. Mr. Don Bliss and the Accelerator Technicians constructed a great deal of the experimental apparatus. The task of scanning the oscilloscope film was enthusiastically performed by Mr. L. Auerbach, Mr. R. Bacastow, Dr. Jim Foote, Mr. J. Lach, Mr. E. Rogers, and Mr. H. Rugge. Additional help was given by Miss Maureen Kane, Mr. K. Nataini, Miss Jean Firby, Miss Francis Wilcox, and Mr. R. Talsma. Finally we wish to thank the Bevatron personnel for their support and cooperation during the experiment.

REFERENCES

*Now at Los Alamos Scientific Laboratory.

1. T. Elioff, L. Agnew, O. Chamberlain, H. M. Steiner, C. Wiegand, and T. Ypsilantis, Phys. Rev. Letters 3, 285, (1959).

2. O. Chamberlain, in Proceedings of the 1960 Annual Internation Conference on High-Energy Physics at Rochester, August 25-September 1, edited by E. C. G. Sudershan et al. (Interscience Publishers, Inc., New York, 1960), p. 653.

3. W. A. Wenzel, in Proceedings of the 1960 Annual International Conference on High-Energy Physics at Rochester, August 25-September 1, (Interscience Publishers, Inc., New York, 1960), p. 151.

4. Coombes, B. Cork, W. Galbraith, G. Lambertson, and W. A. Wenzel, Phys. Rev. 112, 1303 (1958).

5. L. Agnew, T. Elioff, W. Fowler, R. Lander, W. Powell, E. Segrè, H. M. Steiner, H. White C. Wiegand, and T. Ypsilantis, Phys. Rev. 118, 1371 (1960).

6. N. Horwitz, D. Miller, J. Murray, and R. Tripp, Phys. Rev. 115, 472 (1959).

7. G. Goldhaber, S. Goldhaber, W. Powell, and R. Silberberg, Phys. Rev. 121, 1525 (1961).

8. O. Chamberlain, D. Keller, R. Mermod, E. Segrè, H. Steiner, and T. Ypsilantis, Phys. Rev. 108, 1553 (1957).

9. B. Cork, G. Lambertson, O. Piccioni, and W. Wenzel, Phys. Rev. 107, 248 (1957).

10. J. Ball and G. Chew, Phys. Rev. 109, 1385 (1958).

11. Z. Koba and G. Takeda, Progr. Theoret. Phys. (Kyoto) 19, 269 (1958).

12. L. Agnew, O. Chamberlain, D. Keller, R. Mermod, E. Rogers, H. Steiner, and C. Wiegand, Phys. Rev. 108, 1550 (1957).

13. O. Chamberlain, D. Keller, E. Segrè, H. Steiner, and C. Wiegand, Phys. Rev. 102, 1637 (1956).

14. Owen Chamberlain, Ann. Rev. Nuclear Sci. 10, 161 (1960).

15. Harold Ticho, Proceedings of the International Conference on High-Energy Accelerators and Instrumentation, CERN 1959 (CERN Scientific Information Service, Geneva, 1959), p. 390.

16. H. G. Jackson, D. A. Mack, and C. Wiegand, IRE Trans. on Nuclear Science NS-6, 64 (1959).

17. O. Chamberlain and C. Wiegand, Proceedings of the CERN Symposium on High-Energy Accelerators and Pion Physics, Vol. II (CERN Scientific Information Service, Geneva, 1956), p. 82.

18. Edwin McMillan, Rev. Sci Instr. 22, 117 (1951).

19. O. Chamberlain, W. Chupp, G. Goldhaber, E. Segrè, C. Wiegand, E. Amaldi, G. Baroni, C. Castagnoli, C. Franzinetti, and A. Manfredini, Nuovo cimento 3, 462 (1956).

20. R. Hagedorn, Nuovo cimento 15, 246 (1960).

21. O. Chamberlain, E. Segrè, C. Wiegand, and T. Ypsilantis, Phys. Rev. 100, 947 (1955).

22. V. Cocconi, T. Fazzini, G. Fidecaro, M. Legros, N. Lipman, A. Merrison, Phys. Rev. Letters 5, 19 (1960).

23. L. Gilly, B. Leontic, A. Lundby, R. Meunier, J. Stroot, and M. Szeptycka, Proceedings of the 1960 Annual International Conference on High-Energy Physics at Rochester (Interscience Publishers, New York, 1960), p. 808.

24. R. Armenteros, C. Coombes, B. Cork, G. Lambertson, and W. Wenzel, Phys. Rev. 119, 2068 (1960).

25. S. Fernbach, R. Serber, and T. B. Taylor, Phys. Rev. 75, 1352 (1949).

26. F. Solmitz, Proceedings of the 1960 Annual International Conference on High-Energy Physics at Rochester, (Interscience Publishers, New York, 1960) p. 168.

27. N. Xuong, G. Lynch, C. K. Hinrichs, Phys. Rev. 124, 575 (1961).

28. W. Barita, Phys. Rev. 104, 222 (1956).

29. J. Lannutti, G. Lynch, B. Maglić, M. L. Stevenson, and N. Xuong, Proceedings of the 1960 Annual International Conference on High-Energy Physics at Rochester (Interscience Publishers, New York), p. 160.

30. Bipin R. Desai, Phys. Rev. 119, 1390 (1960).

31. C. Keith Hinrichs, Charge-Exchange Production of Antineutrons, Lawrence Radiation Laboratory Report UCRL-9589, March 1961 (unpublished).

32. G. Baroni, C. Belletini, C. Castagnoli, M. Ferro-Luzzi, and A. Manfredini, Nuovo cimento 12, 564 (1959).

33. J. Button, T. Elioff, E. Segrè, H. Steiner, R. Wiengart, C. Wiegand, and T. Ypsilantis, Phys. Rev. 108, 1557 (1957).

34. S. Gartenhaus, Phys. Rev. 107, 291 (1957).

35. P. Signell and R. Marshak, Phys. Rev. 109, 1229 (1958).

36. G. Chew, Proc. National Acad. Sci. U. S. 45, 456 (1958).

37. D. Yennie, M. Levy, and D. Ravenhall, Revs. Modern Phys. 29, 144 (1957).

38. Geoffrey Chew, in Proceedings of the 1958 International Conference on High-Energy Physics at CERN, edited by B. Ferretti, (CERN Scientific Information Service, Geneva, 1958), p. 106.

39. F. Tamm, Soviet Physics JETP 5, 154 (1957).

40. Burton J. Moyer, in Physics Division Semiannual Report, Aug. 1959, Lawrence Radiation Laboratory Report UCRL-8936 (unpublished), p. 33.

41. Meshcheriakov, Bogachev, Leksin, Naganov, and Piskarev, in Proceedings of the CERN Symposium on High-Energy Accelerators and Pion Physics, Vol. II (CERN Scientific Information Service Geneva, 1956), p. 124.

42. R. Glauber, Phys. Rev. 100, 242 (1955).

43. R. Cool, O. Piccioni, and D. Clark, Phys. Rev. 103, 1082 (1956).

44. F. Chen, C. Leavitt, and A. Shapiro, Phys. Rev. 103, 211 (1956).

45. J. S. Blair, Nuclear Phys. 6, 348 (1958).

46. R. Glauber, Lectures in Theoretical Physics (Interscience Publishers, New York, 1959), p. 378.

47. J. Ball and J. Fulco, Phys. Rev. 113, 647 (1959).

48. E. Segrè, Annual Rev. Nuclear Sci. 8, 127 (1958).

49. I. Pomeranchuk, Soviet Physics JETP 3, 306 (1956).

50. I. Pomeranchuk, Soviet Physics JETP 7, 499 (1958).

51. G. von Dardel, D. Frish, R. Mermod, R. Milburn, P. Piroue, M. Vivargent, G. Weber, and K. Winter, Phys. Rev. Letters 5, 333 (1960).

52. S. Lindenbaum, W. Love, J. Niederer, S. Ozaki, J. Russel, L. Yuan Phys. Rev. Letters 7, 184 (1961).

Table I. Experimental components of Fig. 1.

Symbol	Component description
T	Bevatron target area.
W	Thin window of Bevatron vacuum system (0.020-in. Al).
C	Brass collimator, 6 in. diam by 8 in. thick.
M1, M2	60-in.-long deflection magnets with 12-by-7-in. aperture (θ_{M1} = 17 deg, θ_{M2} = 25 deg).
Q1, Q2, Q3	Sets of quadrupole focusing magnets, 8-in. aperture.
S_1	Plastic scintillation counter, 3-1/2 in.-diam.by 1/4 in. thick.
S_2	Plastic scintillation counter 3-1/16 in.-diam. by 1/4 in. thick.
VSC II	Antiproton narrow-band velocity-selecting Cerenkov counter utilizing cyclohexene radiator, (n = 1.46, ρ = 0.8 g/ml) 3-1/4-in.-diam. by 4.7 in. long. The velocity resolution $\Delta\beta$ = 0.03 in the range 0.95 >β>0.70.
$\bar{C}$	Meson Cerenkov counter utilizing the same radiator as VSCII, but views only Cerenkov light that is totally reflected internally, i.e., for β>0.95.
S_3	Plastic scintillation counter, 5 in. diam. by 3/8 in. thick.
A	Area for hydrogen target and final counter system.

Table II. Production of antiprotons of various momenta by 6-Bev protons.

Momentum (Mev/c)	Angle of emission (deg)(lab)	Target length (cm)	Target material	π^-/p^+ [a] (10^{-7})	$\bar{p}/\pi^-$ [a] (10^{-5})	$\bar{p}/p^+$ [b] (10^{-11})
1200	5	5.08	carbon	12.6	1.8±0.1	13.8±0.8[c]
1400	3	5.08	carbon	11.2	2.9±0.2	22.1±1.5[c]
1531	1.5	5.08	carbon	11.8	3.5±0.3	34.7±2.1[c]
1684	0	5.08	carbon	11.8	3.8±0.2	39.2±1.6[c]
1825	1.5	5.08	carbon	11.9	3.6±0.3	37.4±2.2[c]
1700	0	15.3	beryllium	13.0	4.5±0.5[d]	
2000	0	15.3	beryllium	12.0	4.8±0.5[d]	
2800	0	15.3	beryllium	9.0	2.9±0.9[d]	
750	8.5	15.3	beryllium	8.0	0.2±0.12[e]	
900	3	15.3	beryllium	12.0	0.4±0.24[e]	
1150	2.5	15.3	beryllium	20.0	1.2±0.7[e]	
1410	6.2	15.3	beryllium	22.0	1.9±1.1[e]	
600	0	15.3	beryllium	40.	0.15±0.07[f]	
700	0	15.3	beryllium	50.	0.24±0.12[f]	
800	0	15.3	beryllium	50.	0.44±0.22[f]	
900	7	15.3	beryllium	60.	0.80±0.40[f]	

[a] Transmitted through magnetic channel.

[b] Corrected at carbon target.

[c] This experiment.

[d] Reference 24.

[e] Reference 9.

[f] Reference 4.

Table III. $\bar{p}$-p cross sections at various energies.

$\bar{p}$ energy (Mev)	Cross sections (mb)			
	Total	Elastic	Inelastic	Charge-exchange
534±25	118±6	42±5	70±3	6.0±1.3
700±33	116±5	42±4	66±3	7.2±1.5
816±37	108±5	38±4	63±3	7.1±1.2
948±42	96±3	33±3	56±2	6.8±1.0
1068±46	96±3	30±2	60±2	5.7±1.1

Table IV. Optical-model parameters

$T_{\bar{p}}$ (Mev)	R_0 (10^{-13} cm)	ρ_0 (10^{-13} cm)
534	0.89±0.10	1.04±0.04
758	0.88±0.05	1.00±0.02
1000	0.70±0.04	1.02±0.02
(980)[a]	0.73±0.06	1.03±0.03
(2000)[a]	0.57±0.17	0.98±0.07

[a]Reference 24.

Table V. $\bar{p}$-d cross sections (mb).

$T_{\bar{p}}$ (Mev)	σ_t	σ_e	σ_i	σ_c
534	210±5	80±6	126±5	3.3±1.3
700	189±5	67±5	117±4	5.4±1.4
816	196±6	78±5	112±4	6.5±1.5
948	178±5	71±5	102±4	4.4±1.1
1068	184±3	68±4	109±5	5.6±1.0

Table VI. Evaluations of the $\bar{p}$-n cross sections (mb).

$T_{\bar{p}}$ (Mev)	"$\sigma_i(\bar{p}\text{-}n)$"	C_i	$\sigma_i(\bar{p}\text{-}n)$
534	56±6	23	79±6
700	51±5	20	71±5
816	49±5	19	68±5
948	46±4	17	63±4
1068	49±5	18	67±5

$T_{\bar{p}}$ (Mev)	"$\sigma_t(\bar{p}\text{-}n)$"	C_t	$\sigma_t(\bar{p}\text{-}n)$
534	92±8	27	119±8
700	73±7	23	96±7
816	88±8	24	112±8
948	82±6	20	102±6
1068	88±4	21	109±4

$T_{\bar{p}}$ (Mev)	"$\sigma_e(\bar{p}\text{-}n)$"	$\sigma_e(\bar{p}\text{-}n)$
534	38±8	40±10
700	25±7	25±8
816	40±7	44±9
948	38±6	39±7
1068	38±5	42±6

FIGURE LEGENDS

Fig. 1. Schematic view of the Bevatron experimental area. Components are identified in Table I.

Fig. 2. Oscilloscope photograph of beam-intensity pattern behind the hydrogen target. Each step in the historgram represents 1 cm in the vertical plane.

Fig. 3. Schematic diagram of the VSC-II and $\bar{C}$ counters.

Fig. 4. Efficiency and resolution of the velocity-selecting Cerenkov counter VSC-II for $\bar{p}$ momenta of 1200 and 1640 Mev/c (indicated by the arrows).

Fig. 5. Side view of target-counter system. For clarity, the figure is not shown to exact scale. Container (A) could be filled with liquid hydrogen or deuterium and is a stainless steel cylinder 12 in. long by 6 in. diam with 0.008-in. walls, except for the 0.010-in. Mylar entrance wall. Sixteen scintillation counters, S-1 through S-16, surround container (A) cylindrically. The lead between the target and scintillators is removable. Heat shield (C) is 0.003-in. copper; a thin region (B) of the vacuum wall is 0.035-in. aluminum.

Fig. 6. Schematic view from the beam-exit end of the counter system.

Fig. 7. Simplified block diagram of the basic electronics.

Fig. 8. (a) Position of all possible pulses on oscilloscope film.

(b) Actual photo of five events. All five are seen to have pulses S_1, S_2, S_3, and not $\bar{C}$, thus identifying five incident anti-protons. In the first three events only counters S_4 or S_5, or both, signal, meaning that the antiproton did not interact. In the fourth event the antiproton annihilated, sending pions into counters S3, S4, S10, and S15. In the last event only a single count is detected in S1, which is typical of an elastic scattering into that counter.

Fig. 9. Excitation function for 1684-Mev/c antiprotons produced at 0 deg in carbon. The curves are taken from a statistical model.

Fig. 10. Momentum distribution for antiprotons produced by approx 6-Bev protons on carbon and beryllium. The experimental points are taken from Table II. The curve is calculated by a statistical model.

Fig. 11. Angular distribution of $\bar{p}$-p elastic scattering at 534 Mev.

Fig. 12. Angular distribution of $\bar{p}$-p elastic scattering at 700 and 816 Mev.

Fig. 13. Angular distribution of $\bar{p}$-p elastic scattering near 1 Bev. The 980-Mev points are from Armenteros et al. (reference 24).

Fig. 14. Shown are $\bar{p}$-p cross sections as a function of antiproton kinetic energy. The open symbols are total cross sections; closed symbols are inelastic cross sections (for $T_{\bar{p}} < 288$ Mev they are annihilation cross sections); open symbols encircling a dot are elastic cross section; open symbols crossed by a vertical line at the bottom of the figure are charge-exchange cross sections. The various types of symbols refer to different experiments; the references are correlated with the symbols in the upper right corner of the figure.

Fig. 15. Energy dependence of $\bar{p}$-d cross sections. Square symbol indicates a result from reference 8.

Fig. 16. Comparison of $\bar{p}$-p and $\bar{p}$-n cross sections in the energy range 450 to 1068 Mev.

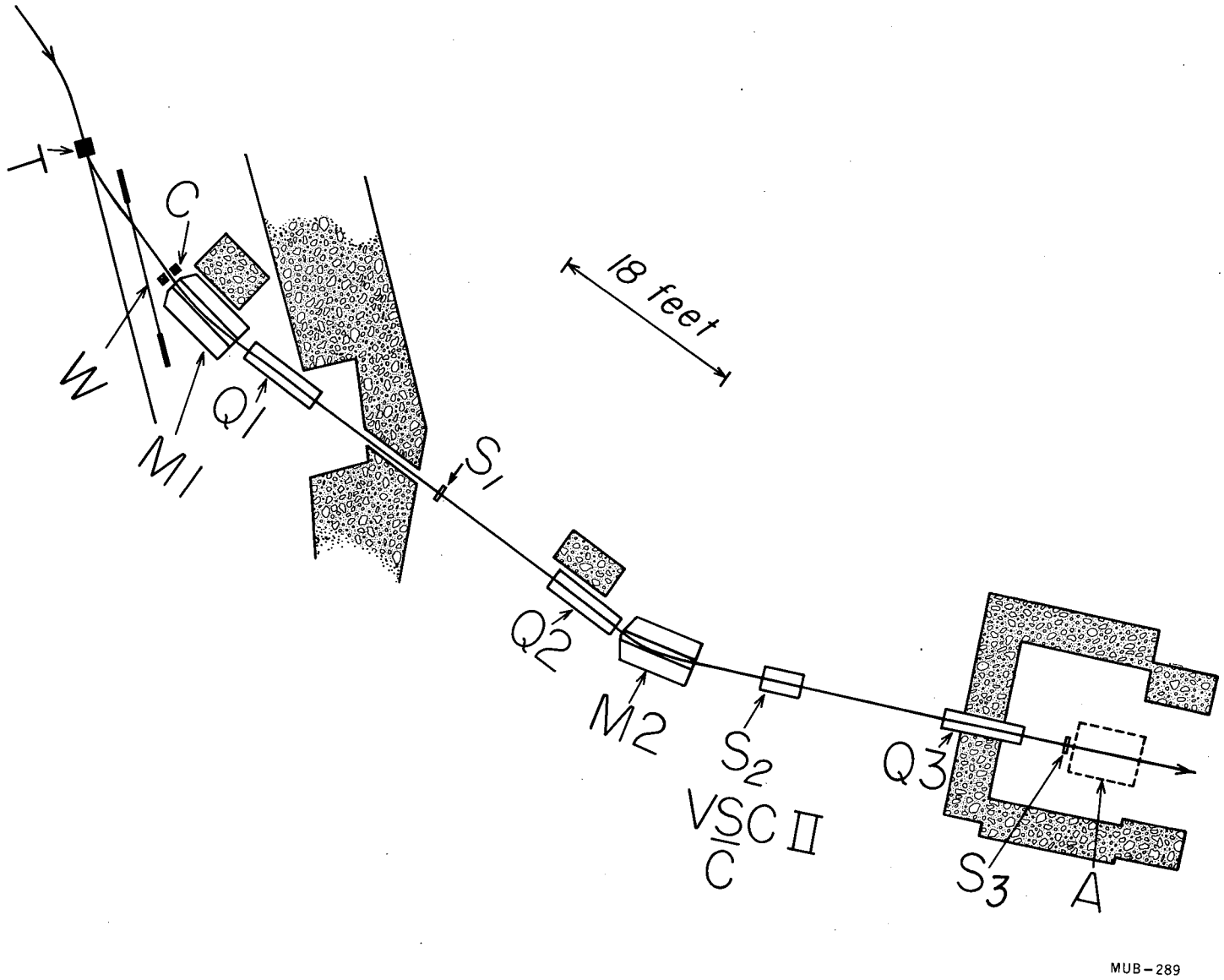

Fig. 1. Schematic view of the Bevatron experimental area. Components are identified in Table I.

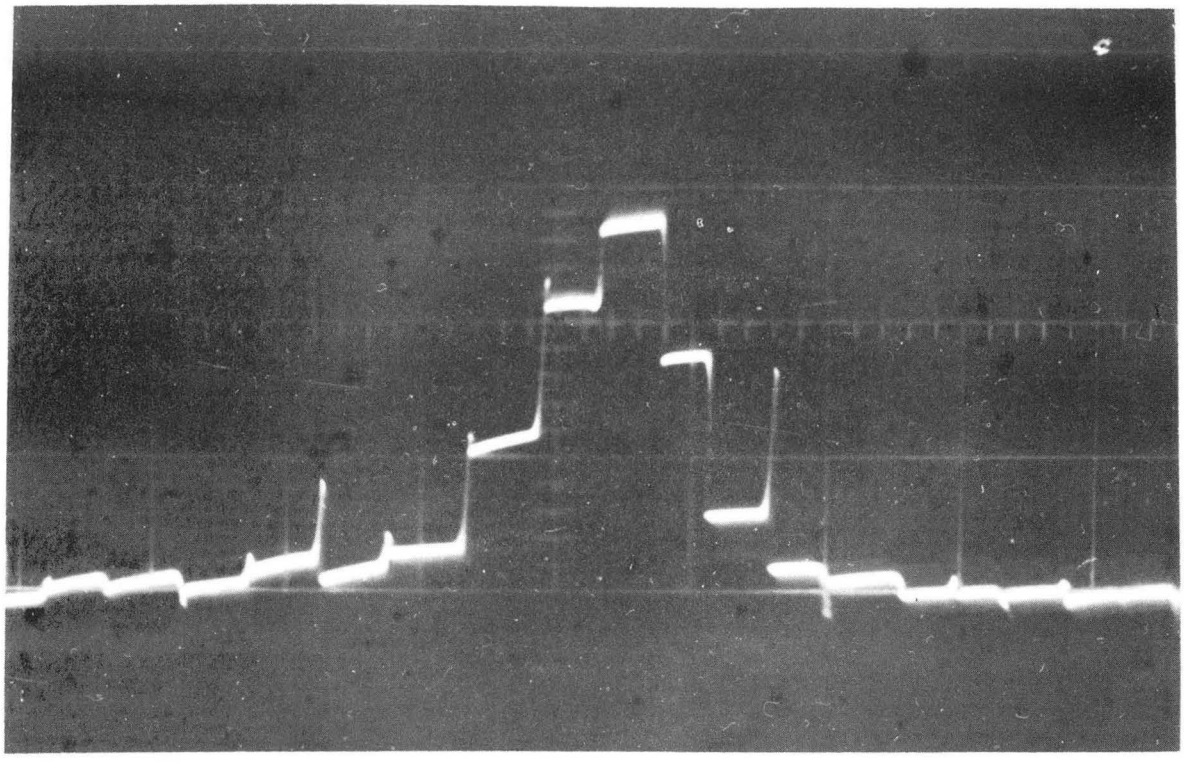

ZN-2553

Fig. 2. Oscilloscope photograph of beam-intensity pattern behind the hydrogen target. Each step in the histogram represents 1 cm in the vertical plane.

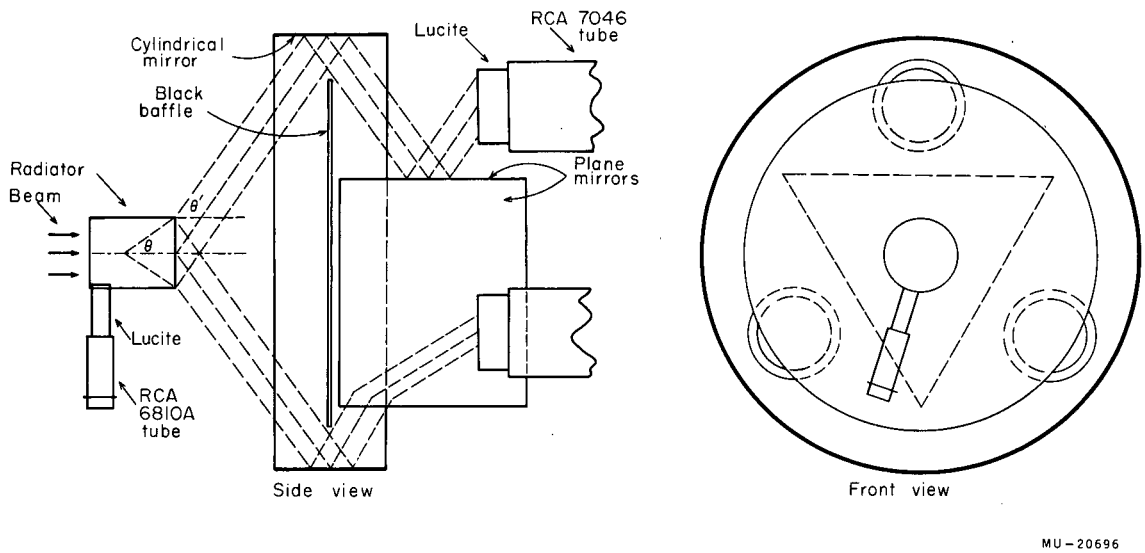

Fig. 3. Schematic diagram of the VSC-II and $\overline{C}$ counters.

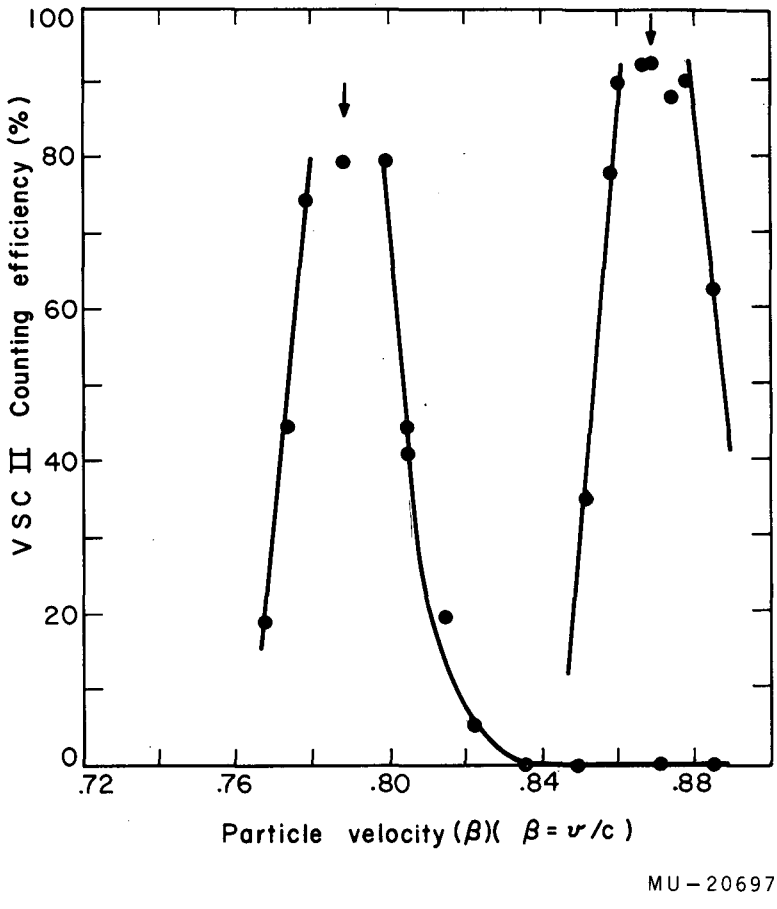

Fig. 4. Efficiency and resolution of the velocity-selecting Cerenkov counter VSC-II for $\bar{p}$ momenta of 1200 and 1640 Mev/c (indicated by the arrows).

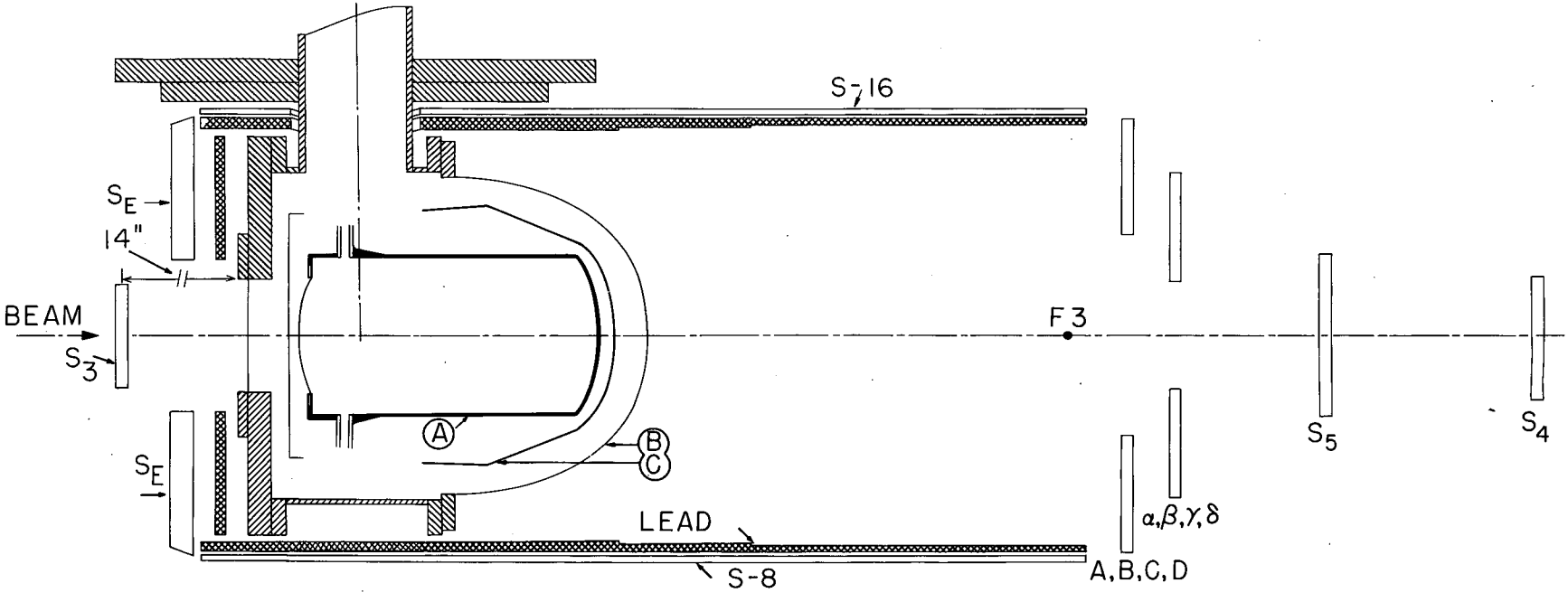

MUB-286

Fig. 5. Side view of target-counter system. For clarity, the figure is not shown to exact scale. Container (A) could be filled with liquid hydrogen or deuterium and is a stainless steel cylinder 12 in. long by 6 in. diam with 0.008-in. walls, except for the 0.010-in. Mylar entrance wall. Sixteen scintillation counters, S-1 through S-16, surround container (A) cylindrically. The lead between the target and scintillators is removable. Heat shield (C) is 0.003-in. copper; a thin region (B) of the vacuum wall is 0.035-in. aluminum.

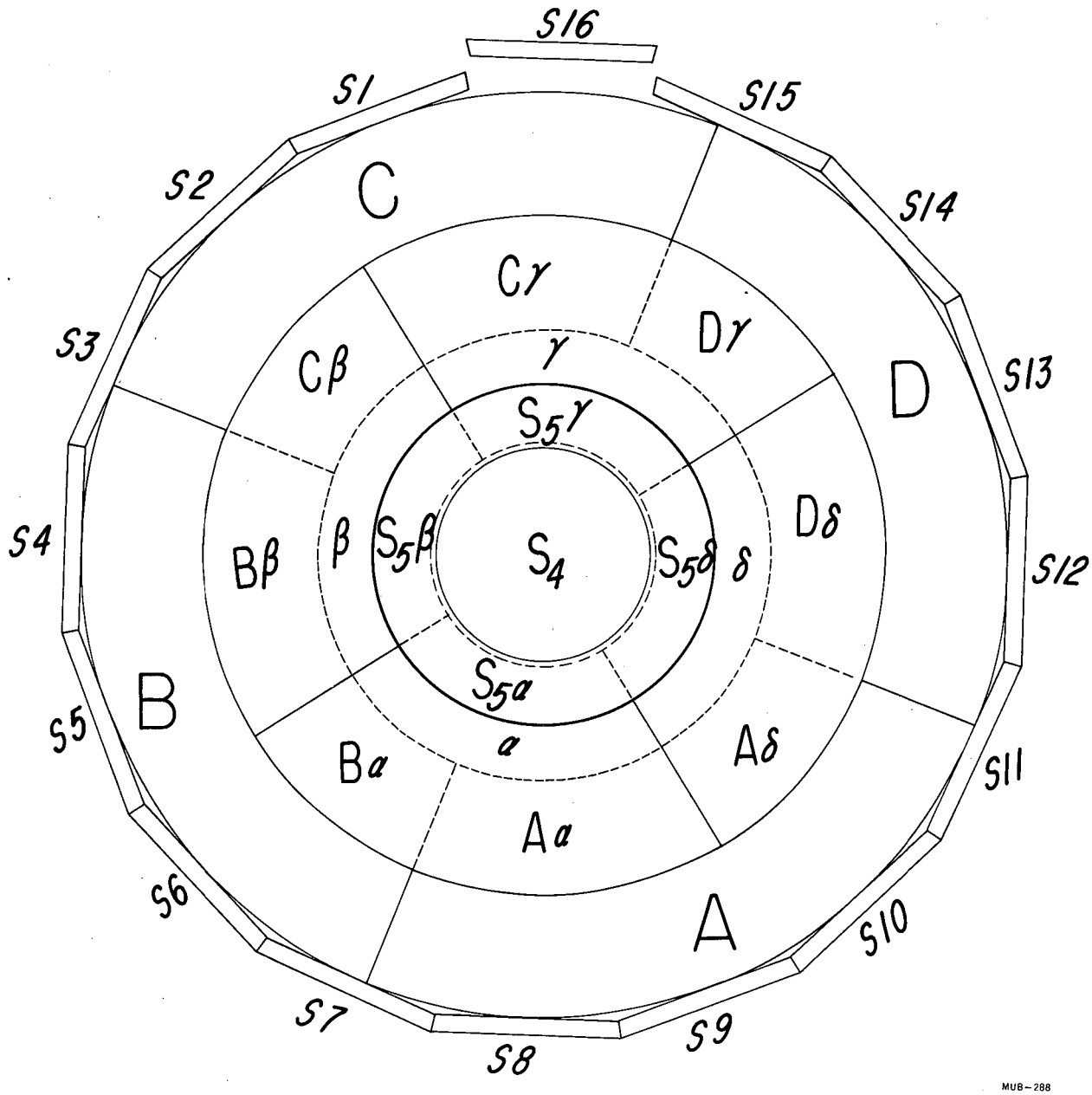

Fig. 6. Schematic view from the beam-exit end of the counter system.

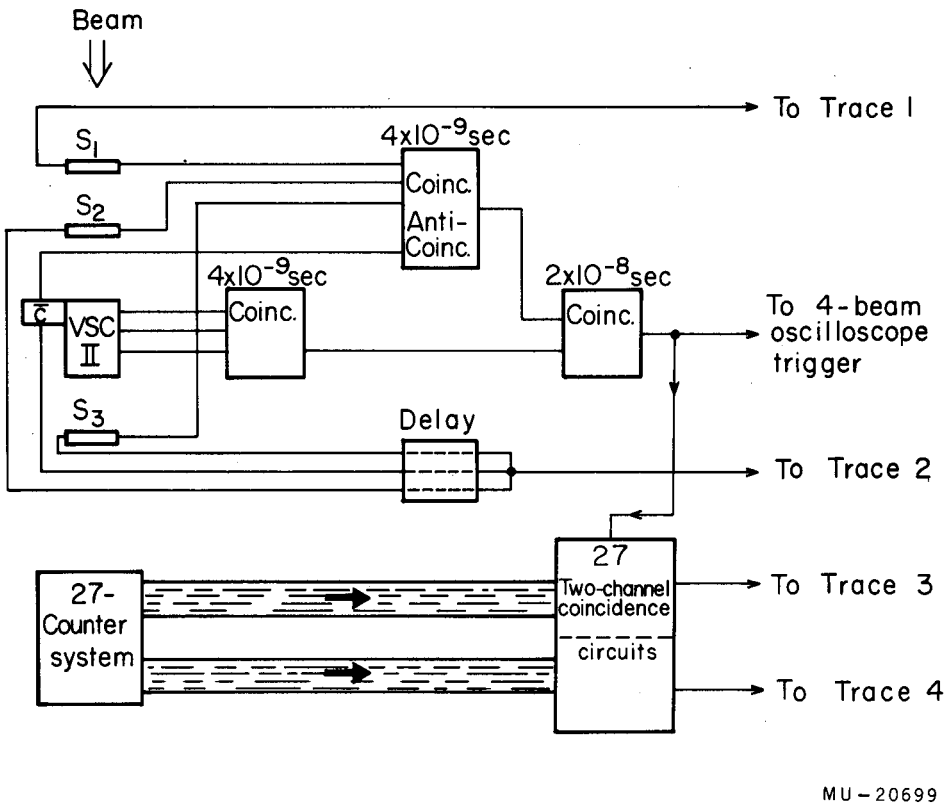

Fig. 7. Simplified block diagram of the basic electronics.

(a)

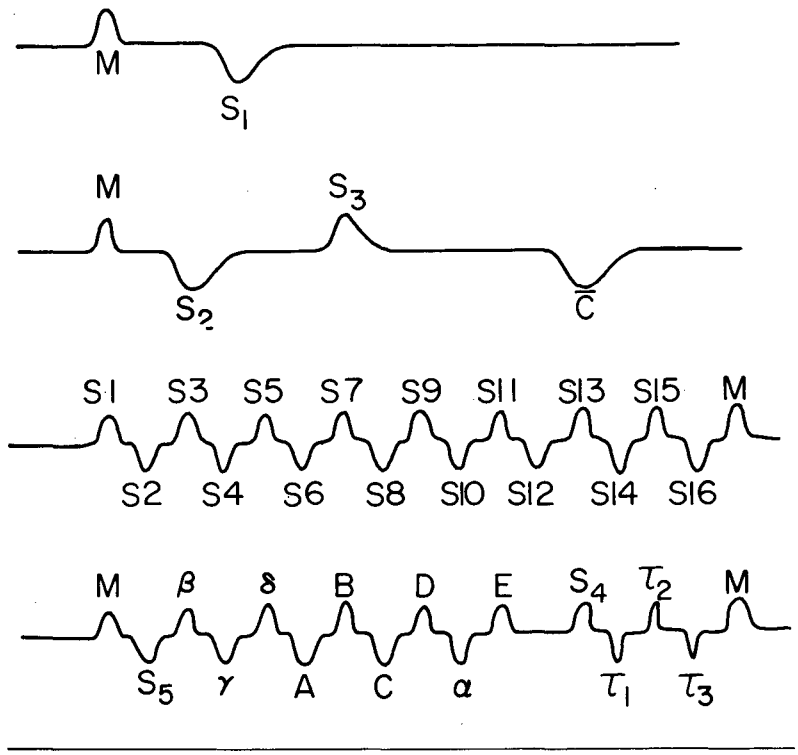

(b)

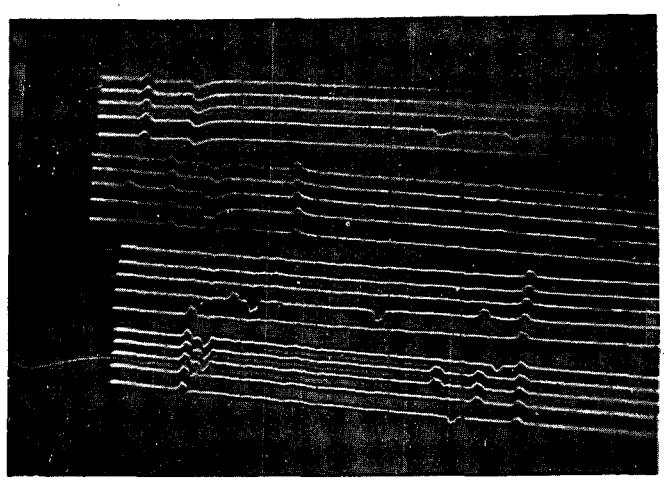

ZN-2555

Fig. 8. (a) Position of all possible pulses on oscilloscope film.

(b) Actual photo of five events. All five are seen to have pulses S_1, S_2, S_3, and not $\bar{C}$, thus identifying five incident protons. In the first three events only counters S_4 or S_5, or both, signal, meaning that the antiproton did not interact. In the fourth event the antiproton annihilated, sending pions into counters S3, S4, S10, and S15. In the last event only a single count is detected in S1, which is typical of an elastic scattering into that counter.

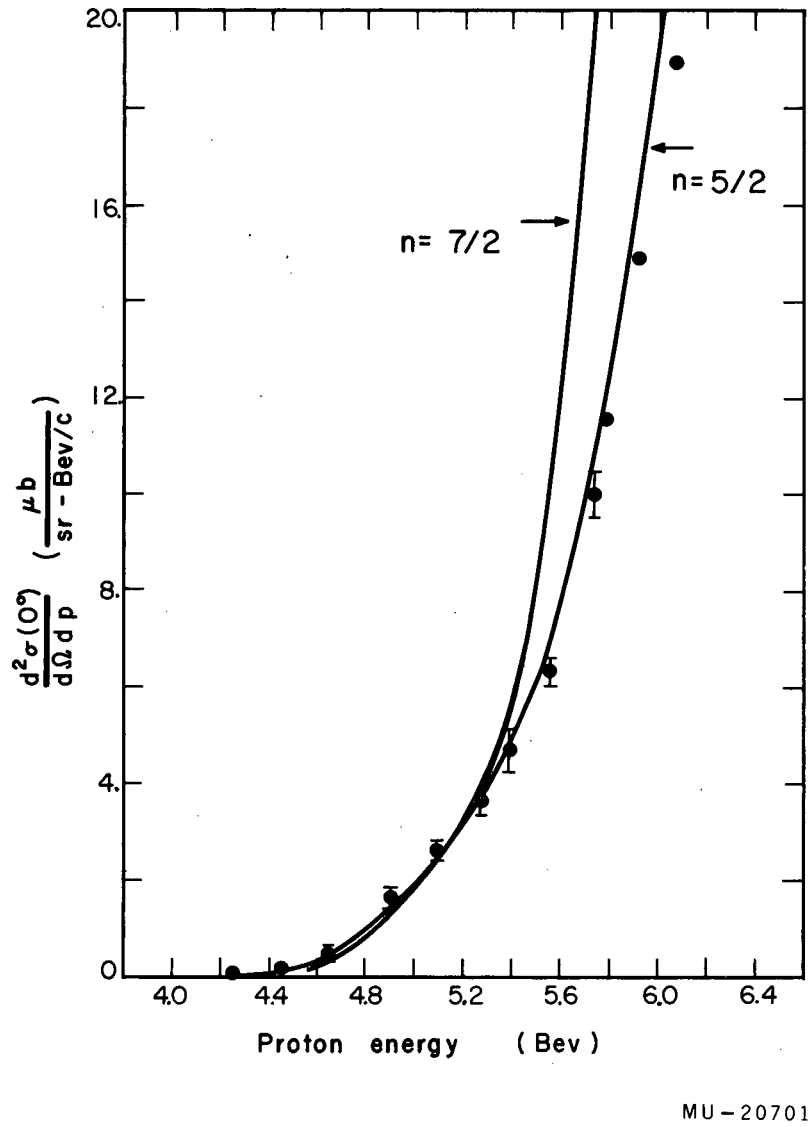

Fig. 9. Excitation function for 1684-Mev/c antiprotons produced at 0 deg in carbon. The curves are taken from a statistical model.

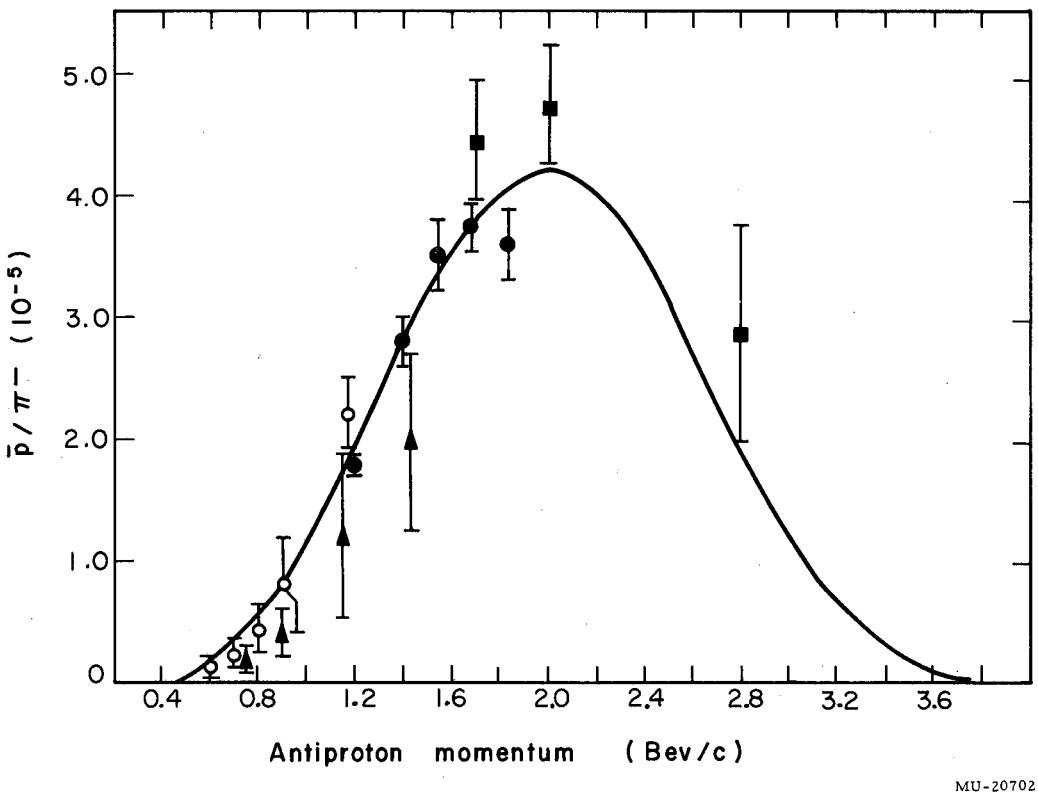

Fig. 10. Momentum distribution for antiprotons produced by approx 6-Bev protons on carbon and beryllium. The experimental points are taken from Table II. The curve is calculated by a statistical model.

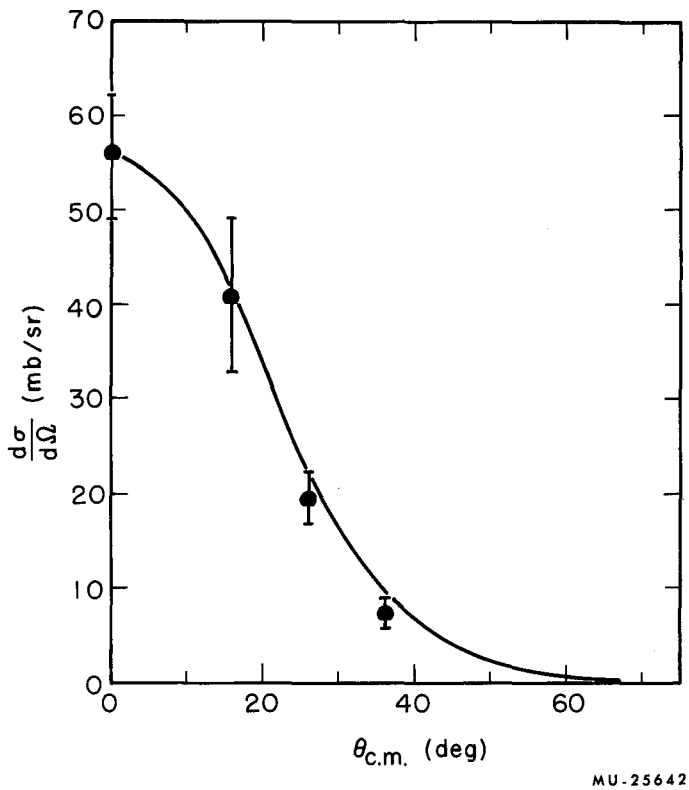

Fig. 11. Angular distribution of $\bar{p}$-p elastic scattering at 534 Mev.

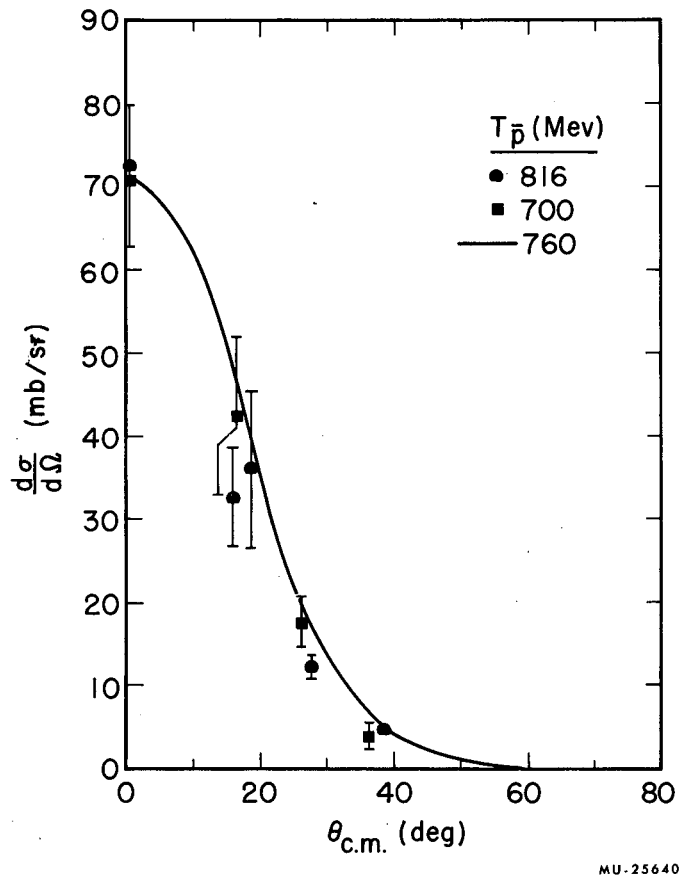

Fig. 12. Angular distribution of $\bar{p}$-p elastic scattering at 700 and 816 Mev.

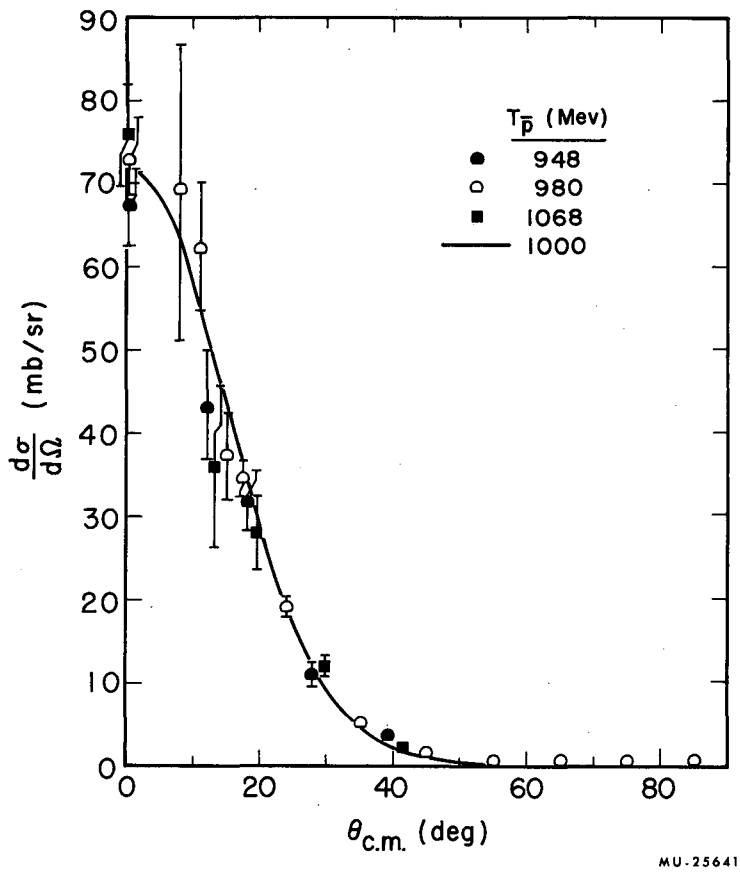

Fig. 13. Angular distribution of $\bar{p}$-p elastic scattering near 1 Bev. The 980-Mev points are from Armenteros et al. (reference 24).

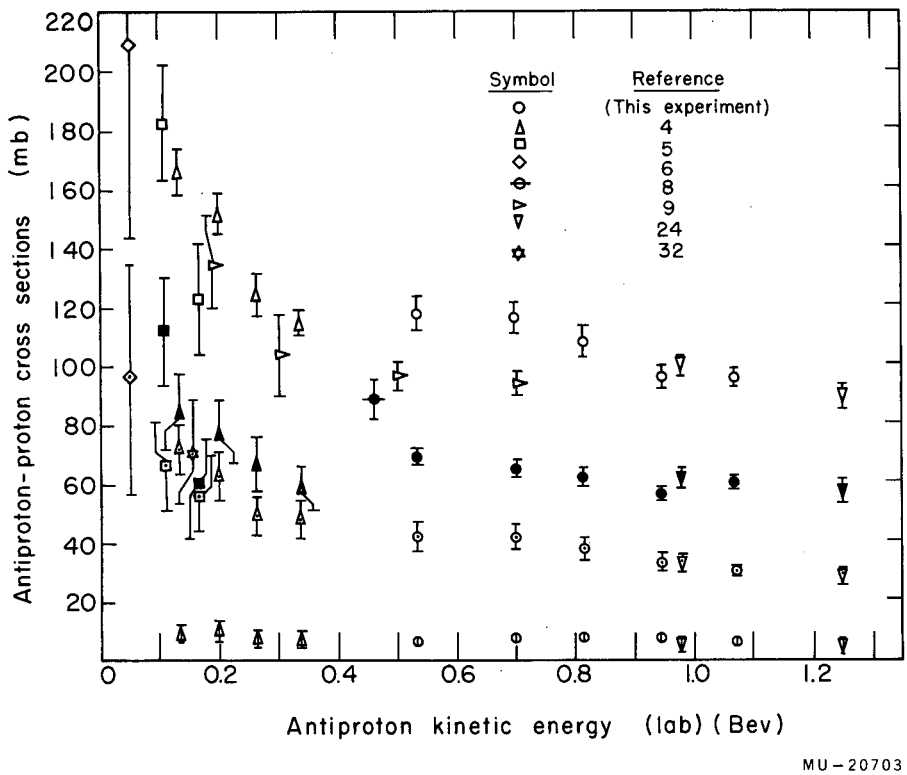

Fig. 14. Shown are $\bar{p}$-p cross sections as a function of antiproton kinetic energy. The open symbols are total cross sections; closed symbols are inelastic cross sections (for $T_{\bar{p}} < 288$ Mev they are annihilation cross sections); open symbols encircling a dot are elastic cross section; open symbols crossed by a vertical line at the bottom of the figure are charge-exchange cross sections. The various types of symbols refer to different experiments; the references are correlated with the symbols in the upper right corner of the figure.

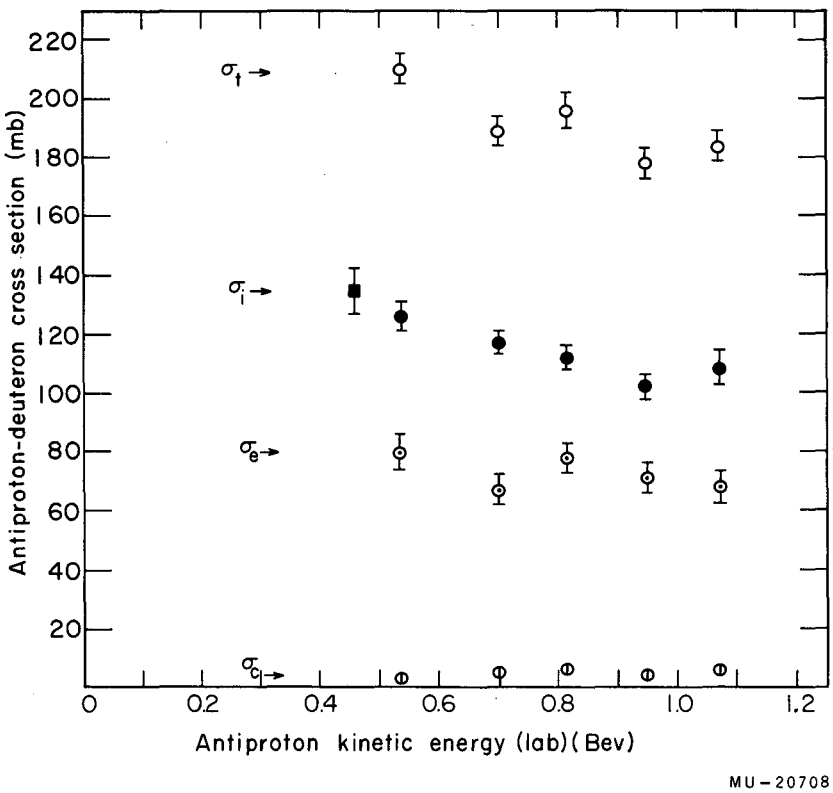

Fig. 15. Energy dependence of $\bar{p}$-d cross sections. Square symbol indicates a result from reference 8.

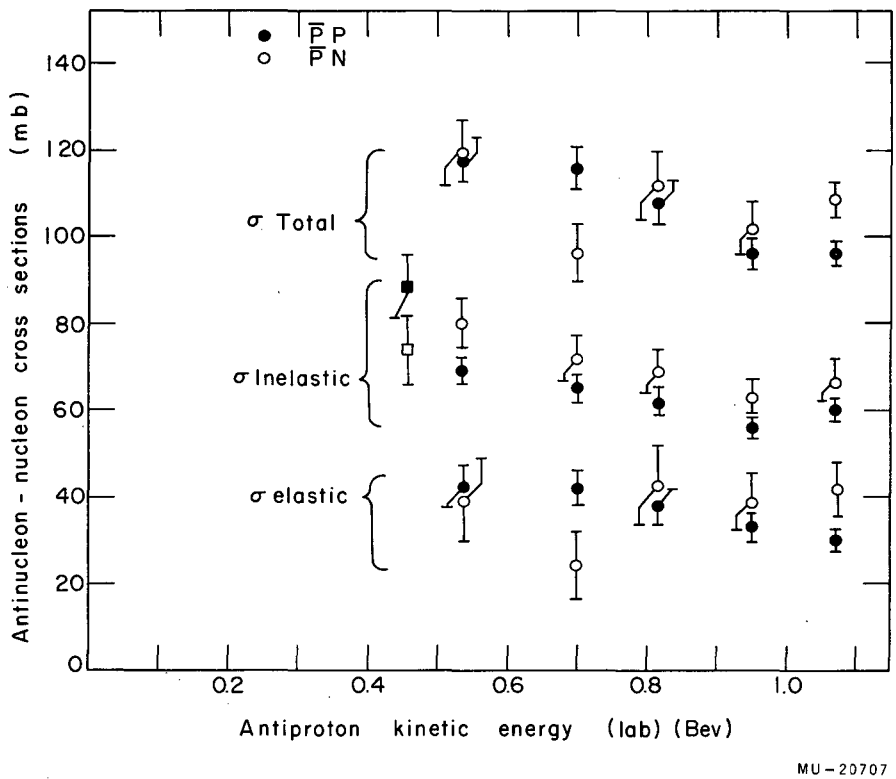

Fig. 16. Comparison of $\bar{p}$-p and $\bar{p}$-n cross sections in the energy range 450 to 1068 Mev.